Luminescence and up-conversion properties in La2Ti2O7:Eu3+,Er3+ oxides under UV and NIR radiations towards a two-color sensor

Fabien Szczepanski, Alexandre Bayart, Arturas Katelnikovas, Jean-François Blach, Jolanta Rousseau, Sébastien Saitzek

▶ **To cite this version:**

Fabien Szczepanski, Alexandre Bayart, Arturas Katelnikovas, Jean-François Blach, Jolanta Rousseau, et al.. Luminescence and up-conversion properties in La2Ti2O7:Eu3+,Er3+ oxides under UV and NIR radiations towards a two-color sensor. Journal of Alloys and Compounds, 2020, 826, pp.154157. 10.1016/j.jallcom.2020.154157 . hal-02567005

HAL Id: hal-02567005
https://hal.science/hal-02567005

Submitted on 7 Mar 2022

HAL is a multi-disciplinary open access archive for the deposit and dissemination of scientific research documents, whether they are published or not. The documents may come from teaching and research institutions in France or abroad, or from public or private research centers.

L'archive ouverte pluridisciplinaire **HAL**, est destinée au dépôt et à la diffusion de documents scientifiques de niveau recherche, publiés ou non, émanant des établissements d'enseignement et de recherche français ou étrangers, des laboratoires publics ou privés.

Distributed under a Creative Commons Attribution - NonCommercial 4.0 International License

Version of Record: https://www.sciencedirect.com/science/article/pii/S092583882030520X
Manuscript_263aeeb32de0543d13841fb6f8716032

Luminescence and up-conversion properties in $La_2Ti_2O_7:Eu^{3+},Er^{3+}$ oxides under UV and NIR radiations towards a two-color sensor

Fabien Szczepanski [1], Alexandre Bayart [1], Arturas Katelnikovas [2], Jean-François Blach [1], Jolanta Rousseau [1], Sébastien Saitzek [1,*]

1 Univ. Artois, CNRS, Centrale Lille, ENSCL, Univ. Lille, UMR 8181, Unité de Catalyse et Chimie du Solide (UCCS), F-62300 Lens, France
2 Institute of Chemistry, Vilnius University, Naugarduko 24, Vilnius LT-03225, Lithuania

***Corresponding author:**

Pr. Sébastien SAITZEK,
[1]Université d'Artois, Unité de Catalyse et de Chimie du Solide, UCCS,
Axe Chimie du Solide, CNRS-UMR 8181, Faculté des Sciences Jean Perrin,

F-62300 LENS, France

Phone: +33 / 321791732, Fax: +33 / 321177955, E-mail: sebastien.saitzek@univ-artois.fr

© 2020 published by Elsevier. This manuscript is made available under the CC BY NC user license
https://creativecommons.org/licenses/by-nc/4.0/

Abstract

$La_{2-x-y}Eu_xEr_yTi_2O_7$ oxides have an emission color which depends on the excitation wavelength. Under the UV excitation (310 to 393 nm), they emit in the red spectral region and, under NIR excitation (785 to 980 nm), they exhibit a green emission induced by upconversion luminescence from Er^{3+} ions. The structural and luminescence properties of these oxides synthesized by the solid state reaction method were studied according to the x and y values. The co-substituted oxides are obtained over a composition zone between $x \leq 0.2$ and $y \leq 0.05$. Beyond these values, a phase mixture consisting of a monoclinic phase (layered-perovskite) and cubic phase (pyrochlore) is observed. Under the UV excitation, the reddish emission color is mainly induced by the Eu^{3+} ions via an exchange interaction mechanism. The quenching concentration of Eu^{3+} ions is dependent on the excitation wavelength: $x = 0.3$ and 0.6, at 310 and 377 nm, respectively. With the measurements of photoluminescence decay curves, the lifetime kinetics was linked to the Eu^{3+} ions concentration. The CIE 1931 color coordinates were also determined according to the x and y values. This one shows linear evolutions when x is fixed and y is variable and vice versa. The good chemical and thermal stability of these oxides also make it possible to disperse them effectively in a glass of lithium tetraborate. Only a 2% transmittance drop is observed for the insertion of 2% wt. of the oxide. The upconversion luminescence properties were also measured under NIR excitation and shown an emission in the green spectral region mainly due to Er^{3+} ions. The study of emission intensity dependence on the laser power led to the conclusion of a two-photon excitation process. Temperature-dependent upconversion emission follows a Mott-Seitz model. The activation energy for $^4F_{9/2} \rightarrow {}^4I_{15/2}$ quenching was found to be 52.8 meV.

1. Introduction

During the last decades, inorganic or hybrid materials with luminescence properties have been widely studied and are currently used in many devices of our daily life [1],[2]. Among these compounds, inorganic materials based on rare earth ions contained in a host-matrixes such as oxides, silicates, aluminates, aluminosilicates, aluminoborates, molybdates, tungstates, etc., are those the most studied by the scientific community [3]. Downconversion (emission in the visible range under a UV light excitation) and upconversion (emission in the visible range under a NIR excitation / absorption of two or more photons) luminescence properties can find many application fields such as fluorescent lamps [4], radiation sensors [5], optical temperature sensors [6], phosphors for LED industry [7], anti-counterfeiting ink [8], incoherent laser light source, display technologies [9], biological labeling [10] and many others [11]. Moreover, the upconverting materials are widely used in biological applications [12] because their excitation wavelength locates within the NIR optical window of biological tissues and it can thus reach the maximum penetration [13]. As such, the upconversion materials are used in the photodynamic therapy [14] or the photoactivated drug delivery systems [15].

Intrinsically, materials that can emit different colors under different types of excitation (UV or NIR) can be particularly attractive for designing multifunctional sensors, anti-counterfeiting inks, multi-color fluorescence imaging or for the biomedical field. Recently, it has been shown that $La_2Ti_2O_7$ oxides can serve as a host matrix for the design of new phosphors with interesting optical properties. Indeed, $La_2Ti_2O_7:Eu^{3+}$ oxides show an intense red emission under UV excitation with a quantum yield of 42% [16]. In addition, we have shown that $La_{1.9}Er_{0.1}Ti_2O_7$ oxide exhibits upconversion luminescence if excited over a wide NIR excitation wavelength range from 785 to 980 nm [17]. In this work, we investigated the possibility to synthesize multifunctional oxides, from a $La_2Ti_2O_7$ host-matrix co-substituted by Eu^{3+}/Er^{3+}, which can respond differently according to the excitation wavelength (UV or

NIR). In the literature and to the best of our knowledge, studies on co-substituted or co-doped $La_2Ti_2O_7$ are scarce. The Yb^{3+}/Er^{3+} system was studied to improve the upconversion properties [18] and the Pr^{3+}/Tb^{3+} system was considered in order to get a control of the emission color [19].

$La_2Ti_2O_7$ is a multifunctional oxide already known for these features: i) piezoelectric and ferroelectric properties with high Curie temperature ($T_c \sim 1500$ °C) [20], [21]; ii) photocatalytic properties, especially used as photocatalyst for H_2 production by water splitting [22],[23] or for Volatile Organic Compounds (VOCs) degradation [24], [25]; iii) luminescence properties when doped or co-doped with other lanthanide ions, such as Pr^{3+}, Sm^{3+}, Eu^{3+}, Er^{3+}, Tb^{3+} [16], [26], [27], [28], [29], [19], [18]; iv) its good resistance to ionizing radiation and its use as an immobilization matrix of radionuclides for the nuclear industry [30]. In the literature, there are several studies that describe techniques for producing $La_2Ti_2O_7$ oxides. Among them, we can mention the solid state reaction, the sol-gel route [31], [32], [33], hydrothermal method [22], floating zone method for single crystals [21] and many others [34], [35], [36]. $La_2Ti_2O_7$ crystallizes in monoclinic/layered perovskite structure with $P2_1$ space group (#4). The unit cell consists of four corner-sharing TiO_6 octahedra separated by two layers of La-site cations along $\vec{c}$-axis and infinite chains of corner-sharing TiO_6 octahedra along $\vec{a}$- and $\vec{b}$-axis. The stability of the monoclinic/layered perovskite structure can be affected during the substitution of La-site by another lanthanide. Indeed, the monoclinic structure is conserved for ionic ratio $r(Ln^{3+})/r(Ti^{4+})$ higher than 1.78 (i.e., Ln^{3+} = La^{3+} to Nd^{3+}). While for $r(Ln^{3+})/r(Ti^{4+})$=1.46 to 1.78 (i.e. Ln^{3+}=Sm^{3+} to Lu^{3+}), a cubic/pyrochlore structure with $Fd\bar{3}m$ space group (#227) is favored [37],[38].

In this work, we have synthesized a series of co-substituted $La_{2-x-y}Eu_xEr_yTi_2O_7$ oxides in order to determine the stability limit of the monoclinic/layered perovskite structure and

study the luminescence properties of these oxides under UV and NIR excitation. For that, the classical luminescence and upconversion measurements (excitation and emission spectra, photoluminescence lifetime, quantum efficiency, thermal quenching mechanisms, and CIE 1931 chromaticity coordinates) were performed.

2. Experimental Section

$La_{2-x-y}Eu_xEr_yTi_2O_7$ oxides were synthesized by a conventional solid state reaction method. The lanthanide oxides (La_2O_3, Eu_2O_3 and Er_2O_3 – 99.99% Strem Chemicals) and titanium dioxide (TiO_2 – 99.99% Sigma Aldrich) were used as starting materials. Before the synthesis, the lanthanide oxides were annealed at 800 °C for 5 h in order to avoid the lanthanum hydroxide formation which could disturb the good stoichiometry of the final product. The precursors weighed in stoichiometric proportions were mixed for 20 min with a few drops of ethanol and then calcined at 1100 °C for 12 h under air. The calcination and milling steps were repeated twice to improve the sample homogeneity.

The X-Ray Diffraction (XRD) measurements were performed using a Rigaku ULTIMA IV diffractometer equipped with Cu anticathode ($\lambda(K_\alpha)$ = 1.5418 Å), Soller slits to limit the divergence of X-ray beam, and a nickel foil filter to attenuate the Cu K_β line. XRD patterns were recorded in the range of 10°-90° (scan speed was 0.1 °/min) using the Bragg-Brentano configuration. The Scanning Electron Microscopy (SEM) images were recorded using Hitachi S4700 microscope equipped with a Field Emission Gun (FEG). The optical properties of $La_2Ti_2O_7:Eu^{3+}$, Er^{3+} oxides were characterized using a UV-2600 spectrophotometer (Shimadzu). Room-temperature excitation and emission spectra were recorded on an Edinburgh Instruments FLS980 spectrometer equipped with a double grating

Czerny-Turner excitation and emission monochromators. For upconversion experiments, two CW (Continuous Wave) lasers emitting at 808 and 980 nm were employed as the excitation sources. The Thermal Quenching (TQ) measurements were performed using a cryostat "MicrostatN" from the Oxford Instruments coupled to the Edinburgh Instruments FLS980 spectrometer. Liquid nitrogen was used as a cooling agent and the measurements were performed at 77 K and at 100–500 K with 50 K steps. The temperature stabilization time was 90 s and the temperature tolerance was set to ±5 K. During the measurements, dried nitrogen was flushed over the cryostat window to avoid the water condensation on the window surface at low temperatures. Finally, the CIE 1931 chromaticity coordinates (Commission Internationale de l'Éclairage – CIE) were calculated from the emission spectra. The color coordinates were calculated in the range of 360-830 nm.

3. Results and Discussions

3.1 Structural and Optical Characterizations

The XRD patterns of $La_{2-x-y}Eu_xEr_yTi_2O_7$ powders are presented in Figure 1. According to the substitution percentage, the $La_2Ti_2O_7$ monoclinic structure (ICSD-1950) [39] is maintained when the Eu^{3+} and Er^{3+} contents in the structure are lower than 0.20 and 0.10, respectively. Beyond these substitution values, a phase mixture of a substituted monoclinic phase and cubic/pyrochlore phases such as $Eu_2Ti_2O_7$ (ICSD-83596) [40] and $Er_2Ti_2O_7$ (ICSD-249070) [41], which are indicated by a star in Figure 1, is obtained. We can note that the presence of a low concentration of Er^{3+} (ca. y=0.05) greatly limits the maximum substitution rate of Eu^{3+}. This one is limited to x = 0.20, whereas, in a previous study [16], it was shown that it could reach 0.60 without Er^{3+} ions. Knowing that, the stability limit of these structures is linked by the value of the Ti^{4+}/Ln^{3+} ionic ratio as indicated in the introductory part. The observed structural feature can, therefore, be explained by the ionic radii values of the

lanthanides (La^{3+}_{VIII} (1.160 Å), Eu^{3+}_{VIII} (1.066 Å) and Er^{3+}_{VIII} (1.004 Å)) [30]. Indeed, the ionic radius of the Er^{3+} ion is lower than that of the Eu^{3+} ion which itself is lower than that of the La^{3+} ion. Therefore, the average ionic radius weighted by the substitution percentages (as Vegard's law [42]) quickly reaches the stability limit of the monoclinic phase. Thus, in the interval [$x \leq 0.20$; $y \leq 0.10$], a single phase isostructural with $La_2Ti_2O_7$ oxide is observed. The substitution is evidenced by the slight displacement of the (hkl) diffraction peaks towards the wide angle, reflecting a decrease of the unit cell volume. According to x and y values, this displacement is clearly observed for (hkl) reflections with h and $k \neq 0$ (enlargement shown in Figures 1c and 1d), while the position of the (00*l*) reflection is not affected. This behavior, already observed for mono-substitution, can be explained by the layered-perovskite structure. Indeed, it is formed by an infinite sequence of TiO_6 octahedra along $\vec{a}$- and $\vec{b}$-axes and sheets consisting of four TiO_6 octahedra separated by an Ln-interleaves along the $\vec{c}$-axis. Thus, the decrease of the ionic radius of the lanthanide ion has a great influence on the infinite chains of octahedra, explaining the evolution of the *a* and *b* cell parameters. Consequently, the Ln-interleaves placed between sheets are placed in a less dense layer which can be modified to counterbalance the cationic modification and permits to explain the relative stability of the *c* cell parameter. In addition, Zhang *et al.* [43] have shown that the $La_2Ti_2O_7$ had a high compressibility along the $\vec{c}$-axis. This direction is, therefore, less sensitive to the modification of the ionic radius and also makes it possible to explain the stability of the *c* cell parameter.

The morphology of $La_{2-x-y}Eu_xEr_yTi_2O_7$ observed by SEM images are presented in Figure 2. For the low substitution rates (Figure 2a and 2b), aggregates consisting of uniform particles of submicron size are observed with homogenous grain-size distribution. When the substitution rates increase, the grain-size distribution becomes more random (Figure 2c and 2d) probably reflecting the multiphasic character observed in the XRD experiments. For substantial substitutions of La by Eu and Er elements (in order to avoid the detection limit),

the Energy Dispersive X-Ray (EDX) analyzes confirm also a uniform distribution of La, Ti, Eu and Er elements in the matrix (corresponding to the values expected by the stoichiometric calculations).

The optical properties of $La_{2-x-y}Eu_xEr_yTi_2O_7$ phosphors were characterized by UV-visible diffuse reflectance spectra. The absorption spectra were recorded for all samples. In Figure 3, the typical room temperature absorption spectra for $La_{1.85}Eu_{0.10}Er_{0.05}Ti_2O_7$, $Eu_2Ti_2O_7$ and $Er_2Ti_2O_7$ oxides are shown. Except $Eu_2Ti_2O_7$ sample, each transition assignment in the spectra corresponds to the excited level of Er^{3+} ions starting from the ground state $^4I_{15/2}$. So, the transitions bands centered at 378, 454, 466, 522, 538, 653 and 798 nm correspond to $^4G_{11/2}$, $^4F_{3/2;\ 5/2}$, $^4F_{7/2}$, $^2H_{11/2}$, $^4S_{3/2}$, $^4F_{9/2}$ and $^4I_{9/2}$ of Er^{3+} energy levels, respectively [44]. For $Eu_2Ti_2O_7$ oxide, the intensities of absorption lines, attributable to the excited states of Eu^{3+} ions, are very low. In order to identify them, it is necessary to zoom at the base of peak starting at 350 nm (inset of Figure 3a). The broad and intensive absorption band in the range of 200–340 nm occurs due to Eu^{3+}-O^{2-} Charge Transfer (CT) transition. The sets of lines centered at 394, 465, 427 and 589 nm correspond to transitions originating from the $^7F_{0,1}$ ground state of Eu^{3+} ions to $^5L_6$, $^5D_2$, $^5D_1$ and $^5D_0$ excited states, respectively [45]. $La_2Ti_2O_7$ oxide is a semi-conductor material, thus, the optical band-gap (E_g) can be determined by the Tauc plot based on the following equation [42]:

$$\alpha h\nu = A(h\nu - E_g)^n \quad (1)$$

Here α is the absorption coefficient, $h\nu$ corresponds to the photon energy, A is a proportionality constant and E_g represents the optical band-gap. Finally, the exponent n denotes the nature of the transition. Here, $La_2Ti_2O_7$ compound is known to have a direct allowed transition; thus, the equations were solved with n = ½ [46]. As illustrated in Figure 3b, the $(\alpha h\nu)^2$ vs. $h\nu$ plots, allow to determine the effective optical band-gaps by extrapolating the linear region of the curves to the $h\nu$ axis intercept. We observed that the E_g values are very

close and decrease slowly with the decrease of the Ln^{3+} ionic radius. The E_g values are 3.85, 3.78 and 3.77 eV for $La_{1.85}Eu_{0.10}Er_{0.05}Ti_2O_7$, $Eu_2Ti_2O_7$ and $Er_2Ti_2O_7$, respectively.

3.2 Luminescence properties

The room-temperature (RT) excitation and emission spectra recorded in the range from 250 to 800 nm for a $La_{1.6}Eu_{0.10}Er_{0.30}Ti_2O_7$ compound are shown in Figure 4. The spectra presented are typical of those recorded on the complete range of $La_{2-x-y}Eu_xEr_yTi_2O_7$ oxides whose evolution in normalized intensity is showed in supplementary materials (Figure S1). First, in the excitation spectrum, two overlapped broad bands are observed around 280 and 310 nm, which can be attributed to the host-related absorption due to the Inter Valence Charge Transfer (IVCT) and the charge transfer (CT) of Eu^{3+}/Er^{3+}-O^{2-}, respectively [19] (in correlation with the previous optical band-gap measurements). Depending on the emission wavelength, two different behaviors with many transition bands are observed. These transitions, corresponding to the intra-configurational f-f transitions of Eu^{3+} and Er^{3+} ions, can be indexed using the Dieke diagram [47]. For $\lambda_{em} = 612.5$ nm, the transitions observed are mostly due to the excited levels of Eu^{3+} ions (i.e., $^7F_0 \rightarrow {}^5D_4$ (361 nm), $^7F_0 \rightarrow {}^5L_{7,8}$; ^5G_J (375 nm), $^7F_0 \rightarrow {}^5L_6$ (396 nm), $^7F_1 \rightarrow {}^5D_3$ (412 nm) and $^7F_0 \rightarrow {}^5D_2$ (465 nm)), while for $\lambda_{em} = 547.5$ nm the transitions originating from Er^{3+} ions are also rather highlighted (i.e., by $^4I_{15/2} \rightarrow {}^4G_{7/2}$ (355 nm), $^4I_{15/2} \rightarrow {}^2K_{15/2}$; $^4G_{9/2}$ (364 nm), $^4I_{15/2} \rightarrow {}^4G_{11/2}$ (377 nm), $^4I_{15/2} \rightarrow {}^2H_{9/2}$ (406 nm)). In the same way, the emission spectra differ according to the excitation wavelength. Under $\lambda_{exc} = 310$ nm, many transitions with the most intense line centered at 612.5 nm (orange-red spectral range) are observed. These lines can be assigned to Eu^{3+} transitions between the lowest excited $^5D_0$ levels and ^7F_J (J = 0 – 5) ground state [48], [49], [50]. The splitting of spectral lines is undoubtedly due to a modification of the electronic states by a Stark effect [51]. Under $\lambda_{exc} = 377$ nm, two green emission bands centered at 525

and 548 nm are observed. These bands correspond to the $^2H_{11/2} \rightarrow {}^4I_{15/2}$ and $^4S_{3/2} \rightarrow {}^4I_{15/2}$ transitions of Er^{3+} ions, respectively [52]. In addition, at $\lambda_{exc} = 377$ nm, the ratio between emissions in the green and red ranges varies greatly depending on the x and y values within the $La_{2-x-y}Eu_xEr_yTi_2O_7$ oxides. Thus, a shift of the emission towards the green spectral domain is observed only for Er^{3+} concentrations greater than y = 0.10 and for very low concentrations of Eu^{3+} ($x \leq 0.10$), as highlighted on the Figure S1 (Supplementary Material). Beyond this x value, the emission is mainly in the orange-red spectral range. The emission is, therefore, mainly dominated by the effect of Eu^{3+} ions within $La_2Ti_2O_7$ host matrix. Further, under $\lambda_{exc} = 310$ nm, only orange-red emission is observed regardless the x and y values.

In Figure 5a, a photograph displaying the emission color of $La_{2-x-y}Eu_xEr_yTi_2O_7$ oxides under the excitation of commercial UV excitation lamp (365 nm) is presented. One can note a difference in intensity that is visible to the naked eye according to the values of x and y. In order to quantify this evolution in the luminescence intensity, we plotted the intensity variations of several emission bands under several excitation wavelengths as a function of the x and y values. The intensity evolution of the $^4S_{3/2} \rightarrow {}^4I_{15/2}$ transition at three excitation wavelengths (i.e., 310, 377 and 393 nm) is presented in Figure 5b. The first result indicates that this transition is active only for an excitation wavelength of 377 nm and that its intensity increases progressively with the Er^{3+} ions concentration. The excitation at other mentioned wavelengths resulted in weak to no emission of Er^{3+} ions. This also indicates that the emission due to Eu^{3+} ions dominates mainly under the UV excitation. The intensity evolution of $^5D_0 \rightarrow {}^7F_2$ (the most intense) and $^5D_0 \rightarrow {}^7F_4$ transitions under the 310 and 377 nm excitation is presented in Figure 5c in order to highlight the x influence and in Figure 5d to highlight the y influence. In the case of $La_{1.95-x}Eu_xEr_{0.05}Ti_2O_7$ oxides, the intensity of the transitions observed goes through a maximum which is different according to the excitation. These are x = 0.30 and x = 0.60 for 310 and 377 nm, respectively. This difference in the quenching concentration

254 can be explained by an energy transfer between the Er^{3+} and Eu^{3+} ions. Under the excitation at
255 310 nm, only the Eu^{3+} ions act as activators while under an excitation at 377 nm, the Eu^{3+} and
256 Er^{3+} ions are both activators. Therefore, under an excitation at 377 nm, the concentration
257 quenching appears later than it in the case of a mono-substituted oxide. In a previous study
258 [16], we showed that for mono-substitution with Eu^{3+}, the quenching concentration is reached
259 for x = 0.8, that is close to the value determined here. In the case of the oxide $La_{1.90-y}Eu_{0.10}Er_yTi_2O_7$, the intensity values of the $^5D_0 \rightarrow {}^7F_2$ and $^5D_0 \rightarrow {}^7F_4$ transitions decrease
261 when the y value increases. Note that for λ_{exc} = 377 nm, the relative intensity is significantly
262 lower than that observed for the 310 nm excitation. This also confirms that there is an energy
263 transfer between the Er^{3+} and Eu^{3+} ions at this wavelength.

264 In addition, we can estimate the critical distance (R_c) by the following formula given by
265 Blasse [53]:

266
$$R_C = 2\left(\frac{3V}{4\pi\, x_C N}\right)^{1/3} \qquad (2)$$

267 Here V is the unit cell volume, x_c represents the concentration of activator ions where the
268 quenching occurs and N is the number of ions whose sites are partially occupied by the
269 activator in the unit cell (in our case $N = 8$). At λ_{exc} = 310 nm and λ_{exc} = 377 nm, x_c is equal to
270 0.175 and 0.325, respectively (sum of Eu^{3+} and Er^{3+} concentration in the oxide). So, the
271 critical transfer distances are about 3.81 and 4.80 Å, respectively. Knowing that the exchange
272 interaction takes place when the critical distance value is about 3 – 4 Å [54], we can conclude
273 that this mechanism is more accentuated under the excitation at 310 nm.

274 The room temperature photoluminescence decay curves of $La_{1.95-x}Eu_xEr_{0.05}Ti_2O_7$
275 phosphors are shown in Figure 6a. The samples were excited at 393 nm and the emission was

monitored at 612.5 nm ($^5D_0 \rightarrow {}^7F_2$ transition). These decay curves can be fitted successfully based on the following multifold exponential equation [55]:

$$I(t) = I_0 \sum_i^N A_i e^{-\frac{t}{\tau_i}} \quad (3)$$

where, I and I_0 correspond to the luminescence intensity at a given time t and initial intensity, respectively. A_i are pre-exponential constants which are related with the initial intensity, τ_i are the lifetimes for the each exponential components. The average fluorescence lifetime τ_{ave} can be calculated by the following equation [56]:

$$\tau_{ave} = \frac{\sum_i^N A_i \tau_i^2}{\sum_i^N A_i \tau_i} \quad (4)$$

In our case, the PL decay curves can be fitted with a double exponential function. We can observe a progressive decrease in average life time values with the Eu^{3+} concentration increase. This evolution can be explained by resonant energy transfer between Eu^{3+} ions (and Er^{3+} ions), what leads to decrease of excited state lifetime.

We can also note that this double-exponential modeling reveals the different environments for Eu^{3+} cations, as explained by the presence of several crystallographic sites in the monoclinic structure.

In addition, Khalil *et al.* [58] have proposed the following equation to describe thermal and concentration quenching [58]:

$$\frac{1}{\tau} = K_t = K_r + K_{nr}(T) + K_C\left[Eu^{3+}\right] \quad (5)$$

Where K_t is the observed decay rate, K_r and $K_{nr}(T)$ are the radiative and non-radiative decay rates, respectively, and K_c is the quenching term dependent on the concentration of europium ions. $K_{nr}(T)$ is dependent on the environment and temperature. This equation can be transposed to our case by adding a component related to the Er^{3+} concentration:

$$\frac{1}{\tau} = K_t = K_r + K_{nr}(T) + K_C\left[Eu^{3+}\right] + K_C^{'}\left[Er^{3+}\right] \quad (6)$$

If we consider that the measurements are carried out at a constant temperature and that the concentration of Er^{3+} ions is constant in samples series, the PL lifetime (or average lifetime) is directly related to the concentration of Eu^{3+} ions according to the equation:

$$\tau_{ave} = \frac{1}{A + K_C[Eu^{3+}]} \quad (7)$$

Where A is a constant. The evolution of an average lifetime as a function of the x is shown in Figure 6b. We find a decay that can satisfy the expression (7) followed by a bearing from x = 0.6. This limit is in good relation with the concentration quenching observed under the 377 nm excitation (see Figure 5c). The average lifetime changes from 894 to 674 µs and K_c can be calculated by modeling the first part of the curve (dashed line in Figure 6b). This one is worth 1.299×10^{-3} μs^{-1}.at. $\%^{-1}$. In the same way, the room temperature PL decay curves of $La_{1.95-y}Eu_{0.10}Er_yTi_2O_7$ monitored at 393 nm and correspondent to the $^5D_0 \rightarrow {}^7F_2$ transition were also acquired. These curves are shown in Figure S2. The τ_{ave} variation of the lifetime as a function of y shows a sudden decrease until y = 0.10, then an increase. This evolution can be related to the structural modification experienced by the sample series (see Figure 1). Indeed, below y = 0.1, only the monoclinic phase is present and, beyond, a phase mixture is obtained (monoclinic and cubic). In order to study the Er^{3+} influence, we also recorded the PL decay curves as a function of x and y for the $^4S_{3/2} \rightarrow {}^4I_{15/2}$ transition (Er^{3+}) excited at 377 nm. The dependences are shown in Figure S3. Besides the fact that these average PL lifetime values are significantly smaller, if compared to those of the $^5D_0 \rightarrow {}^7F_2$ transition of the Eu^{3+} ions, the changes in average PL lifetime values show a sharp fall for low values of x and y. This also tells us that the constant K'_c is much higher than the constant K_c. All these results show a dominance of Eu^{3+} ions on the spectral emission of $La_{2-x-y}Eu_xEr_yTi_2O_7$ oxides.

As observed in the photographs of Figure 5a, the $La_{2-x-y}Eu_xEr_yTi_2O_7$ oxides present an intense emission with orange-reddish color. The CIE 1931 chromaticity coordinates have been calculated for the entire series under $\lambda_{exc} = 310$ nm. In Figure 7a, the 3D plot of CIE 1931 coordinates as a function of the atomic percent of europium ions are shown. On the 2D plot projection, we observe a linear variation between the X and Y coordinates (Figure 7b) which illustrates a change of color from orange to red. This color shift can be explained by an intensity increase of the line coming from the $^5D_0 \rightarrow {}^7F_2$ transition with respect to those of other transitions. In the similar way, the 3D plot of CIE 1931 chromaticity coordinates as a function of the atomic percent of erbium ions are presented in Figure 7c. On the 2D plot projection (Figure 7d), we observe also a linear variation between the X and Y coordinates. This time, we observe a shift from red to orange with the increase in the proportion of erbium. This behavior is explained by a larger intensity decrease for the $^5D_0 \rightarrow {}^7F_2$ line if compared to that of the $^5D_0 \rightarrow {}^7F_1$ line. It is known that the $^5D_0 \rightarrow {}^7F_2$ transition is hypersensitive to the local environment and the $^5D_0 \rightarrow {}^7F_1$ is insensitive to site symmetry [48]. Consequently, the ratio between these emission intensities defined by $R = I(^5D_0 \rightarrow {}^7F_2)/I(^5D_0 \rightarrow {}^7F_1)$, can be used as a sensitive optical probe to determine the symmetry site where Eu^{3+} ion is located [59]. The evolution of the R value is presented in Figure S4 in supplementary materials. We observe a linear decrease of this value between x = 0.01 and x = 0.1 values of Er^{3+} content in synthesized compounds. This can be explained by a lower distortion of the Eu^{3+} ion occupancy sites due to the insertion of Er^{3+} ions within the layered perovskite structure. Indeed, the Er^{3+} ion radius is smaller, it counterbalances the distortion of the sites of occupation in the monoclinic/layered-perovskite structure. Above x = 0.1, a break is observed which may be related to the presence of a phase mixture (monoclinic/cubic), as described in the XRD part. In this case, the cubic phase has centro-symmetric lattice sites that can be occupied by Eu^{3+} ions and, therefore, this also contributes to the decrease of the R ratio.

346 The good thermal resistance and the submicron size of these oxides can allow a homogeneous
347 dispersion in a vitreous matrix to create luminescent glasses for displays, artworks and even
348 anti-counterfeiting markers in luxury flasks. In order to verify this, we carried out a 2% mass
349 dispersion of oxide in a lithium tetraborate matrix. The glass wafer (⌀ 4 cm, thickness 3 mm)
350 is then formed through the fused bead method. As shown in Figure 8, the transmittance of the
351 glass is very slightly affected by the presence of the oxide. The transmittance drop by 2% is
352 observed in the visible range. Photography under natural light, as shown in inset of Figure 8,
353 highlights the good conservation of the glass transparency. Under UV light (365 nm), the
354 luminescence is clearly observed with the naked eye (the intensity increases with the
355 concentration of europium, as observed in the case of oxides). The transmission spectrum also
356 shows characteristic transitions of the Er^{3+} and Eu^{3+} ions, which are directly annotated in
357 Figure 8. The absorption lines, observed in transmission spectrum of the glass sample, are just
358 overlapping, as observed in excitation spectra. The good chemical and thermal resistance of
359 these oxides allows us to use them as active material within vitreous matrix.
360
361 **3.3 Up-conversion luminescence properties**
362 The upconversion properties of $La_{2-x-y}Eu_xEr_yTi_2O_7$ oxides were also investigated using
363 two lasers emitting at 808 and 980 nm. In Figure 9a, the emission of the different powders
364 under a laser excitation of 785 nm (power 40 mW) is shown. All samples showed green
365 luminescence visible by naked eye. It is also evident that brightness of emitted light decreases
366 with increasing Eu^{3+} concentration for a fixed Er^{3+} concentration. The opposite, however, is
367 observed if Er^{3+} concentration is increased for the fixed Eu^{3+} content. This clearly indicate,
368 that high Eu^{3+} concentration quenches upconversion emission of Er^{3+} ions in La_{2-x-}
369 $_yEu_xEr_yTi_2O_7$ oxides. The samples with x = 0.05, y = 0.10 and x = 0.10, y = 0.10 showed the
370 most intensive upconversion luminescence.

The room temperature emission spectra recorded on the $La_{1.70}Eu_{0.20}Er_{0.10}Ti_2O_7$ oxide under the excitation at 980 and 808 nm show three main sets of lines attributable to energy levels of the Er^{3+} ion. The bands centered at 520, 547 and 665 nm correspond to $^2H_{11/2} \rightarrow {}^4I_{15/2}$, $^4S_{3/2} \rightarrow {}^4I_{15/2}$ and $^4F_{9/2} \rightarrow {}^4I_{15/2}$ transitions, respectively (Figure 9b). As the conventional luminescence, the multitude of peaks observed is certainly due to a modification of the electronic states by the Stark effect [51]. The mechanism of absorption in upconversion luminescence can follow three main processes [60], [61]: Excited-State Absorption (ESA), Energy Transfer (ET) and Photon Avalanche (PA). The upconversion mechanisms can be evaluated by measuring the upconversion intensity as a function of the laser power. The number of photons (α) which are required to populate the upper emitting level can be obtained by the following relation [62]:

$$I \propto P^{\alpha} \quad (8)$$

In order to highlight the process involved, we recorded the emission spectra for different laser powers at 980 nm (Figure 9c). Then, we plotted the evolution Ln(I) vs. Ln(P) (see Figure 9d). The slope of this curve indicates the number of photons involved in the absorption process. No inflection point is highlighted, therefore, we can exclude an avalanche process of photons. In our case under the excitation at 980 nm, we observe linear evolutions whose slopes are 1.23 and 1.50 for the $^4S_{3/2} \rightarrow {}^4I_{15/2}$ and $^4F_{9/2} \rightarrow {}^4I_{15/2}$ transitions, respectively. We can suggest that two photons are required to create these mechanisms. This process has already been demonstrated in a previous study on a monosubstitution of $La_2Ti_2O_7$ with Er^{3+} ions [17].

The time-resolved measurements performed for $^4F_{9/2} \rightarrow {}^4I_{15/2}$ transitions under the 980 and 808 nm laser excitation are presented in Figure 10, and this reveals that the main excitation mechanism for Er^{3+} ions is excited state absorption regardless the excitation

wavelength. The decay curve can be fitted using the sum of two exponential functions, as described above. Concerning the $^4F_{9/2} \rightarrow {}^4I_{15/2}$ transition for the 980 nm laser excitation, we obtained an average PL lifetime value of 61.6 μs, and, concerning the same transition for the 808 nm laser excitation, the average PL lifetime value of 32.3 μs is obtained. It is evident that Er^{3+} emission quenches almost twice faster if samples are excited with the 808 nm laser. Therefore, it can be concluded that the internal efficiency of Er^{3+} is higher for the 980 nm laser excitation.

To complete this study, the temperature-dependent upconversion emission spectra of $La_{1.75}Eu_{0.20}Er_{0.05}Ti_2O_7$ specimen were recorded under the laser excitation at 980 nm and they are shown in Figure 11a. The conventional emission spectra with the emission bands attributable to $^2H_{11/2} \rightarrow {}^4I_{15/2}$, $^4S_{3/2} \rightarrow {}^4I_{15/2}$, $^4F_{9/2} \rightarrow {}^4I_{15/2}$ and $^4I_{9/2} \rightarrow {}^4I_{15/2}$ transitions, located at 520, 544, 660 and 811 nm, respectively, are observed. For all transitions, we can see a gradual decrease in intensity as a function of temperature over a range of 77 to 500 K. This decrease is induced by thermal quenching effect. This luminescence quenching is due to the increased probability of non-radiative transitions from excited state to ground state at elevated temperatures [63]. The temperature dependence of the luminescence can be described by the Mott-Seitz equation (E_a represents the activation energy for the thermal quenching) [64], [65]:

$$I(T) = \frac{I_0}{1 + Ce^{-\frac{E_a}{k_B T}}} \tag{9}$$

Where, I_0 and $I(T)$ are the initial intensity and the intensity at the given temperature, respectively. C is constant, k_B is Boltzmann's constant (8.617×10^{-5} eV/K) and E_a is the thermal activation energy for the non-radiative transition. Note that, in this expression of the luminescence decay, the contribution of the phonon-assisted transitions is neglected. The activation energy can be calculated from a plotting of $\ln[(I_0/I)-1]$ against $1/k_BT$, where a slope is equal to $-E_a$. The activation energy for $^4F_{9/2} \rightarrow {}^4I_{15/2}$ transition quenching was found to be

52.8 meV as shown in the inset of Figure 11b. There are several mechanisms that can describe this thermal quenching phenomenon. The most common is based on energy level diagram evolving with the temperature. At low temperature, the excited levels are populated and their de-excitation leads essentially to the emission of luminescence. At high temperature, the phonon frequency increases leading to increased probability of multi-phonon relaxation and thus, non-radiative de-excitation of excited states.

By normalizing the emitted intensity at 544 nm, we clearly observe an evolution of the intensities corresponding to the $^2H_{11/2} \rightarrow {}^4I_{15/2}$ (I_H) and $^4S_{3/2} \rightarrow {}^4I_{15/2}$ (I_S) transitions with temperature (Figure S5a in supplementary material). Therefore, the Fluorescence Intensity Ratio ($FIR(T)=I_H/I_S$) can be employed in thermal sensing [66]. Indeed, the $^2H_{11/2}$ and $^4S_{3/2}$ levels are in thermal equilibrium and the electrons in them obey Boltzmann distribution law; therefore, *FIR(T)* can be expressed by the following equation [67]:

$$FIR(T) = \frac{I_H}{I_S} = A\exp\left(\frac{-\Delta E}{k_B T}\right) \tag{10}$$

Where A is a pre-exponential constant, ΔE is the energy gap separating the $^2H_{11/2}$ and $^4S_{3/2}$ levels, k_B is the Boltzmann constant, and T is the absolute temperature. The calculated values of I_H/I_S as a function of temperature for $La_{1.75}Er_{0.05}Eu_{0.20}Ti_2O_7$ sample are shown in supplementary material (Figure S5b). The fit of experimentally obtained data with this previous equation yielded $\Delta E = 565 \pm 28$ cm^{-1} and $A = 4.539 \pm 0.8$. From there, the sensitivity (S) that defines the change rate of R(T) per unit temperature, can be determined with following equation [68]:

$$S(T) = \frac{dFIR(T)}{dT} = A\exp\left(\frac{-\Delta E}{k_B T}\right)\left(\frac{\Delta E}{k_B T^2}\right) \tag{11}$$

Since the values of A and ΔE were already obtained, it was possible to model the sensitivity curve. So, as shown in supplementary materials (Figure S5c), the sensitivity reaches maximum of $3.1x10^{-3}$ K^{-1} at 405 K and the optimal temperature range of use is defined where the sensitivity S is higher than half of its maximum value S_{Max} as illustrated in Figure S5c in supplementary materials. In a previous study based on $La_{1.9}Er_{0.1}Ti_2O_7$ oxides (mono-substitution with Er^{3+}), the sensitivity was determined at $1.1x10^{-2}$ K^{-1} at 512 K and the useful temperature range was estimated between 250 and 1373 K [17]. To conclude, these oxides can be used for applications of thermal sensing; but in the case of a co-substitution (Eu^{3+}/ Er^{3+}), the Eu^{3+} ions have a detrimental effect with a reduction of the sensitivity (by a ~3.7 factor for $La_{1.75}Eu_{0.20}Er_{0.05}Ti_2O_7$ oxides) and a reduction in the useful temperature range. This behavior can be explained by non-radiative energy transfer (ET) between energy levels of Er^{3+} and Eu^{3+} ions.

4. Conclusion

The $La_{2-x-y}Eu_xEr_yTi_2O_7$ oxides were successfully synthesized using solid-state reaction. These materials were characterized by X-ray Diffraction, Scanning electron microscopy and fluorescence spectroscopies. We have demonstrated that the monoclinic structure is preserved if Eu^{3+} and Er^{3+} substitution rates are lower than 0.20 and 0.10, respectively. For higher values, a mixture consisting of a substituted monoclinic phase with the layered-perovskite structure and cubic phases, with the pyrochlore structure ($Eu_2Ti_2O_7$ and $Er_2Ti_2O_7$) were found. In addition, the morphological features of $La_{2-x-y}Eu_xEr_yTi_2O_7$ also depends on the substitution rate. For low substitutions, we have noticed the presence of aggregates of uniform submicron sized particles and, when the rates increase, the grain-size distribution becomes random. Concerning the luminescence properties, we note intense lines,

assigned to Eu^{3+} transitions, centered at 612.5 nm when the samples are excited at 310 nm. However, when the materials are excited at 377 nm, we noticed the presence of green emission bands at 525 and 548 nm which correspond to transitions of Er^{3+} ions. Moreover, we noticed the decrease of the average lifetime with the increase of Eu^{3+} ion content, which is explained by a resonant energy transfer between Eu^{3+} and Er^{3+} ions. The CIE 1931 chromaticy coordinates were plotted versus the Eu^{3+} (and Er^{3+}) ions concentration. A shift from red to orange was observed with the increase of Er^{3+} concentration and a shift from orange to red was observed with the increase of Eu^{3+} concentration. The materials were also dispersed in a glass matrix yielding brightly luminescent glass under the UV radiation. The decrease of glass transparency due to phosphor incorporation was negligible. The upconversion luminescence properties were checked by using two laser lines at 808 and 980 nm. For the later, a two photon mechanism was demonstrated and the observed bands correspond to the emission of Er^{3+} ions. The average upconversion life times are 61.6 and 32.3 µs for 980 and 808 nm laser excitation, respectively. The evolution of the upconversion luminescence with the temperature was investigated and it follows a Mott-Seitz behavior. To finish, these oxides having these double luminescence properties under UV and NIR excitation, can have several potential applications: i) their good thermal resistance allows them to be dispersed in a glass matrix in order to create anti-counterfeit bottles for the luxury perfume industry. The dispersion carried out in this study on a borate glass confirms this potential; ii) These oxides could also be used to design inks that can be used for official documents, ticketing and banknotes (their activities under two distinct wavelengths will strengthen the document security); iii) After a toxicological study, these oxides could also be used for applications in biology in particular as materials for labeling or as support materials for phototherapy to activate a drug under the NIR excitation and also be detectable with the UV microscopy surface excitation; iv) as materials for coupled detection of NIR and UV

radiation on the same material or v) more recently, it has been shown that these oxides, in the form of single crystals, have low extinction coefficients in the visible range [69], [70]. As such, the luminescence properties can be used for the design of laser crystals.

Acknowledgments

The work was financially supported by « les Ministères de l'Europe et des Affaires Etrangères (MEAE) et de l'Enseignement Supérieur, de la Recherche et de l'Innovation (MESRI) » and by the Ministry of Education and Science and the National Research Council of Lithuania (PHC Gilibert (N° 373027ZC)). Chevreul Institute (FR 2638)", "Région Nord Pas-de-Calais", "FEDER" and "C'Nano Nord-Ouest competence centre" are also acknowledged for supporting and funding this work. The authors also thank Nora Djelal for SEM analyses.

References

[1] A.H. Kitai, Principles of Luminescence, in: Lumin. Mater. Appl., John Wiley & Sons, Ltd, 2008: pp. 1–18. https://doi.org/10.1002/9780470985687.ch1.
[2] A. Edgar, Luminescent Materials, in: S. Kasap, P. Capper (Eds.), Springer Handb. Electron. Photonic Mater., Springer International Publishing, Cham, 2017: pp. 1–1. https://doi.org/10.1007/978-3-319-48933-9_38.
[3] G. Blasse, B.C. Grabmaier, Luminescent Materials, Springer-Verlag, Berlin Heidelberg, 1994. ISBN 978-3-642-79017-1.
[4] Y.-C. Lin, M. Karlsson, M. Bettinelli, Inorganic Phosphor Materials for Lighting, Top. Curr. Chem. 374 (2016) 21. https://doi.org/10.1007/s41061-016-0023-5.
[5] B. Lee, M. Kim, H.J. Kim, Y.B. Song, W.J. Yoo, S.H. Shin, D.E. Lee, K.W. Jang, Measurement of Gamma-Rays Induced Luminescence Generated in a Sapphire Based Fiber-Optic Radiation Sensor, J. Appl. Math. Phys. 4 (2016) 720–726. https://doi.org/10.4236/jamp.2016.48158.
[6] X. Wang, O.S. Wolfbeis, R.J. Meier, Luminescent probes and sensors for temperature, Chem. Soc. Rev. 42 (2013) 7834–7869. https://doi.org/10.1039/C3CS60102A.
[7] A. Mills, Phosphors development for LED lighting, III-Vs Rev. 18 (2005) 32–34. https://doi.org/10.1016/S0961-1290(05)01052-5.
[8] P. Kumar, S. Singh, B.K. Gupta, Future prospects of luminescent nanomaterial based security inks: from synthesis to anti-counterfeiting applications, Nanoscale. 8 (2016) 14297–14340. https://doi.org/10.1039/C5NR06965C.
[9] H. Zhong, Z. Wang, W. Lu, J. Liu, Y. Wang, Luminescent Materials for 3D Display Technology, in: R.-S. Liu (Ed.), Phosphors Convers. Nano Part. Quantum Dots Their

Appl., Springer Singapore, 2016: pp. 503–523. https://doi.org/10.1007/978-981-10-1590-8_18.
[10] F. Wang, D. Banerjee, Y. Liu, X. Chen, X. Liu, Upconversion nanoparticles in biological labeling, imaging, and therapy, The Analyst. 135 (2010) 1839–1854. https://doi.org/10.1039/c0an00144a.
[11] C. Feldmann, T. Jüstel, C.R. Ronda, P.J. Schmidt, Inorganic Luminescent Materials: 100 Years of Research and Application, Adv. Funct. Mater. 13 (2003) 511–516. https://doi.org/10.1002/adfm.200301005.
[12] A. Gulzar, J. Xu, P. Yang, F. He, L. Xu, Upconversion processes: versatile biological applications and biosafety, Nanoscale. 9 (2017) 12248–12282. https://doi.org/10.1039/C7NR01836C.
[13] S. Chen, X. Liu, T. McHugh, Near-infrared deep brain stimulation via upconversion nanoparticle-mediated optogenetics, in: Opt. Biopsy XVII Real-Time Spectrosc. Imaging Diagn., International Society for Optics and Photonics, 2019: p. 108730W. https://doi.org/10.1117/12.2506055.
[14] H. Qiu, M. Tan, T.Y. Ohulchanskyy, J.F. Lovell, G. Chen, Recent Progress in Upconversion Photodynamic Therapy, Nanomaterials. 8 (2018) 344. https://doi.org/10.3390/nano8050344.
[15] Y. Yang, J. Mu, B. Xing, Photoactivated drug delivery and bioimaging, Wiley Interdiscip. Rev. Nanomed. Nanobiotechnol. 9 (2017) e1408. https://doi.org/10.1002/wnan.1408.
[16] A. Bayart, A. Katelnikovas, J.-F. Blach, J. Rousseau, S. Saitzek, Synthesis, structural and luminescence properties of $(La_{1-x}Ln_x)_2Ti_2O_7$ (Ln=lanthanides) solid solutions, J. Alloys Compd. 683 (2016) 634–646. https://doi.org/10.1016/j.jallcom.2016.05.041.
[17] A. Bayart, F. Szczepanski, J.F. Blach, J. Rousseau, A. Katelnikovas, S. Saitzek, Upconversion luminescence properties and thermal quenching mechanisms in the layered perovskite $La_{1.9}Er_{0.1}Ti_2O_7$ towards an application as optical temperature sensor, J. Alloys Compd. (2018). https://doi.org/10.1016/j.jallcom.2018.02.055.
[18] S. Tabanli, M. Erdem, B. Canturk, A. Mergen, G. Eryurek, Solid State Synthesis, Structural and Up-Conversion Properties of Yb^{3+}/Er^{3+} and $Yb^{3+}/Tm^{3+}/Er^{3+}$ Doped $La_2Ti_2O_7$ Phosphors, in: B. Di Bartolo, L. Silvestri, M. Cesaria, J. Collins (Eds.), Quantum Nano-Photonics, Springer Netherlands, Dordrecht, 2018: pp. 449–451. https://doi.org/10.1007/978-94-024-1544-5_54.
[19] H. Zhang, G. Li, Y. Zhu, S. Liu, K. Li, Y. Liang, Color tuning and white light emission in a single-phased $La_2Ti_2O_7:Pr^{3+}$, Tb^{3+} phosphor, J. Alloys Compd. 798 (2019) 800–809. https://doi.org/10.1016/j.jallcom.2019.05.306.
[20] H. Yan, H. Ning, Y. Kan, P. Wang, M.J. Reece, Piezoelectric Ceramics with Super-High Curie Points, J. Am. Ceram. Soc. 92 (2009) 2270–2275. https://doi.org/10.1111/j.1551-2916.2009.03209.x.
[21] S. Nanamatsu, M. Kimura, K. Doi, S. Matsushita, N. Yamada, A new ferroelectric: $La_2Ti_2O_7$, Ferroelectrics. 8 (1974) 511–513. https://doi.org/10.1080/00150197408234143.
[22] H. Song, T. Peng, P. Cai, H. Yi, C. Yan, Hydrothermal synthesis of flaky crystallized $La_2Ti_2O_7$ for producing hydrogen from photocatalytic water splitting, Catal. Lett. 113 (2007) 54–58. https://doi.org/10.1007/s10562-006-9004-6.
[23] K. Onozuka, Y. Kawakami, H. Imai, T. Yokoi, T. Tatsumi, J.N. Kondo, Perovskite-type $La_2Ti_2O_7$ mesoporous photocatalyst, J. Solid State Chem. 192 (2012) 87–92. https://doi.org/10.1016/j.jssc.2012.03.055.

[24] W.-M. Hou, Y. Ku, Synthesis and characterization of $La_2Ti_2O_7$ employed for photocatalytic degradation of reactive red 22 dyestuff in aqueous solution, J. Alloys Compd. 509 (2011) 5913–5918. https://doi.org/10.1016/j.jallcom.2011.03.042.
[25] D.W. Hwang, K.Y. Cha, J. Kim, H.G. Kim, S.W. Bae, J.S. Lee, Photocatalytic Degradation of CH_3Cl over a Nickel-Loaded Layered Perovskite, Ind. Eng. Chem. Res. 42 (2003) 1184–1189. https://doi.org/10.1021/ie020457c.
[26] X. Li, H. Cai, L. Ding, X. Dou, W. Zhang, Synthesis and luminescence properties of $La_2Ti_2O_7:Er^{3+}$ nanocrystals with pyrochlore structure, J. Alloys Compd. 541 (2012) 36–40. https://doi.org/10.1016/j.jallcom.2012.07.017.
[27] M. Li, X.Y. Su, Y.M. Yang, L. Liu, F. Yu, X. Li, B. Han, J. Wu, H.J. Seo, Synthesis and Photoluminescence Properties of $La_2Ti_2O_7:Pr^{3+}/Tb^{3+}$ Phosphors, Sci. Adv. Mat. 9 (2017) 587. https://doi.org/info:doi/10.1166/sam.2017.2346.
[28] Z. Shao, S. Saitzek, J.-F. Blach, A. Sayede, P. Roussel, R. Desfeux, Structural Characterization and Photoluminescent Properties of $(La_{1-x}Sm_x)_2Ti_2O_7$ Solid Solutions Synthesized by a Sol–Gel Route, Eur. J. Inorg. Chem. 2011 (2011) 3569–3576. https://doi.org/10.1002/ejic.201100309.
[29] P.T. Diallo, P. Boutinaud, R. Mahiou, Anti-Stokes luminescence and site selectivity in $La_2Ti_2O_7:Pr^{3+}$, J. Alloys Compd. 341 (2002) 139–143. https://doi.org/10.1016/S0925-8388(02)00098-1.
[30] R.D. Shannon, Revised effective ionic radii and systematic studies of interatomic distances in halides and chalcogenides, Acta Crystallogr. Sect. A. 32 (1976) 751–767. https://doi.org/10.1107/S0567739476001551.
[31] Z. Shao, S. Saitzek, P. Roussel, O. Mentré, F. Prihor Gheorghiu, L. Mitoseriu, R. Desfeux, Structural and dielectric/ferroelectric properties of $(La_{1-x}Nd_x)_2Ti_2O_7$ synthesized by sol–gel route, J. Solid State Chem. 183 (2010) 1652–1662. https://doi.org/10.1016/j.jssc.2010.05.004.
[32] A.V. Prasadarao, U. Selvaraj, S. Komarneni, A.S. Bhalla, Sol-gel synthesis of Ln_2(Ln = La, Nd)Ti_2O_7, J. Mater. Res. 7 (1992) 2859–2863. https://doi.org/10.1557/JMR.1992.2859.
[33] V.V. Atuchin, T.A. Gavrilova, J.-C. Grivel, V.G. Kesler, Electronic structure of layered ferroelectric high- k titanate $La_2Ti_2O_7$, J. Phys. Appl. Phys. 42 (2009) 035305. https://doi.org/10.1088/0022-3727/42/3/035305.
[34] D.S. Todorovsky, R.V. Todorovska, M.M. Milanova, D.G. Kovacheva, Deposition and characterization of $La_2Ti_2O_7$ thin films via spray pyrolysis process, Appl. Surf. Sci. 253 (2007) 4560–4565. https://doi.org/10.1016/j.apsusc.2006.10.016.
[35] M. Suresh, A.V. Prasadarao, S. Komarneni, Mixed Hydroxide Precursors for $La_2Ti_2O_7$ and $Nd_2Ti_2O_7$ by Homogeneous Precipitation, J. Electroceramics. 6 (2001) 147–151. https://doi.org/10.1023/A:1011464902626.
[36] P.A. Fuierer, R.E. Newnham, $La_2Ti_2O_7$ Ceramics, J. Am. Ceram. Soc. 74 (1991) 2876–2881. https://doi.org/10.1111/j.1151-2916.1991.tb06857.x.
[37] Z. Shao, S. Saitzek, P. Roussel, R. Desfeux, Stability limit of the layered-perovskite structure in $Ln_2Ti_2O_7$ (Ln = lanthanide) thin films grown on (110)-oriented $SrTiO_3$ substrates by the sol–gel route, J. Mater. Chem. 22 (2012) 24894–24901. https://doi.org/10.1039/C2JM34729F.
[38] S. Saitzek, Z. Shao, A. Bayart, P. Roussel, R. Desfeux, Microstructure and Nanoscale Piezoelectric/Ferroelectric Properties in $Ln_2Ti_2O_7$ (Ln= Lanthanide) Thin Films with Layered Perovskite Structure, in: P. Granger, V.I. Parvulescu, V.I. Parvulescu, W. Prellier (Eds.), Perovskites Relat. Mix. Oxides, Wiley-VCH Verlag GmbH & Co. KGaA, 2016: pp. 233–258.

http://onlinelibrary.wiley.com/doi/10.1002/9783527686605.ch11/summary (accessed January 6, 2017).
[39] M. Gasperin, Dititanate de lanthane, Acta Crystallogr. B. 31 (1975) 2129–2130. https://doi.org/10.1107/S0567740875007005.
[40] E.H. Chtoun, L. Hanebali, P. Garnier, Analyse par diffraction des rayons x, méthode de rietveld, de la structure des solutions solides $(1-x)A_2Ti_2O_7$ - xFe_2TiO_5 A= Eu, Y, Ann. Chim. Sci. Matér. 26 (2001) 27–32.
[41] G.C. Lau, B.D. Muegge, T.M. McQueen, E.L. Duncan, R.J. Cava, Stuffed rare earth pyrochlore solid solutions, J. Solid State Chem. 179 (2006) 3126–3135. https://doi.org/10.1016/j.jssc.2006.06.007.
[42] J. Tauc, Optical properties and electronic structure of amorphous Ge and Si, Mater. Res. Bull. 3 (1968) 37–46. https://doi.org/10.1016/0025-5408(68)90023-8.
[43] F.X. Zhang, J. Lian, U. Becker, R.C. Ewing, L.M. Wang, J. Hu, S.K. Saxena, Structural change of layered perovskite $La_2Ti_2O_7$ at high pressures, J. Solid State Chem. 180 (2007) 571–576. https://doi.org/10.1016/j.jssc.2006.11.022.
[44] B. Zhou, Z. Xiao, A. Huang, L. Yan, F. Zhu, J. Wang, P. Yin, H. Wang, Effect of Tm–Er concentration ratio on the photoluminescence of Er–Tm:Al_2O_3 thin films fabricated by pulsed laser deposition, Prog. Nat. Sci. 18 (2008) 661–664. https://doi.org/10.1016/j.pnsc.2008.01.009.
[45] P.S. Peijzel, A. Meijerink, R.T. Wegh, M.F. Reid, G.W. Burdick, A complete 4f{sup n} energy level diagram for all trivalent lanthanide ions, J. Solid State Chem. 178 (2005). https://doi.org/10.1016/j.jssc.2004.07.046.
[46] T. Pussacq, H. Kabbour, S. Colis, H. Vezin, S. Saitzek, O. Gardoll, C. Tassel, H. Kageyama, C. Laberty Robert, O. Mentré, Reduction of $Ln_2Ti_2O_7$ Layered Perovskites: A Survey of the Anionic Lattice, Electronic Features, and Potentials, Chem. Mater. 29 (2017) 1047–1057. https://doi.org/10.1021/acs.chemmater.6b03808.
[47] G.H. Dieke, H.M. Crosswhite, H. Crosswhite, Spectra and energy levels of rare earth ions in crystals, Interscience Publishers, New York, 1968.
[48] N. Ben Amar, T. Koubaa, M.A. Hassairi, I. Kbaïli, M. Dammak, Optical spectroscopy of Eu^{3+} ions doped in $YAl_3(BO_3)_4$ crystal, J. Lumin. 160 (2015) 95–100. https://doi.org/10.1016/j.jlumin.2014.11.045.
[49] Z. Sun, Q. Zhang, Y. Li, H. Wang, Thermal stable $La_2Ti_2O_7$:Eu^{3+} phosphors for blue-chip white LEDs with high color rendering index, J. Alloys Compd. 1 (2010) 338–342. https://doi.org/10.1016/j.jallcom.2010.06.203.
[50] V.V. Atuchin, A.S. Aleksandrovsky, O.D. Chimitova, T.A. Gavrilova, A.S. Krylov, M.S. Molokeev, A.S. Oreshonkov, B.G. Bazarov, J.G. Bazarova, Synthesis and Spectroscopic Properties of Monoclinic α-$Eu_2(MoO_4)_3$, J. Phys. Chem. C. 118 (2014) 15404–15411. https://doi.org/10.1021/jp5040739.
[51] J. Rocha, L.D. Carlos, J.P. Rainho, Z. Lin, P. Ferreira, R.M. Almeida, Photoluminescence of new Er^{3+}-doped titanosilicate materials, J. Mater. Chem. 10 (2000) 1371–1375. https://doi.org/10.1039/A910192F.
[52] J. Zhang, X. Wang, W.-T. Zheng, X.-G. Kong, Y.-J. Sun, X. Wang, Structure and luminescence properties of TiO_2:Er^{3+} nanocrystals annealed at different temperatures, Mater. Lett. 61 (2007) 1658–1661. https://doi.org/10.1016/j.matlet.2006.07.093.
[53] G. Blasse, Energy transfer in oxidic phosphors, Phys. Lett. A. 28 (1968) 444–445. https://doi.org/10.1016/0375-9601(68)90486-6.
[54] H. Liu, L. Liao, Z. Xia, Structure, luminescence property and energy transfer behavior of color-adjustable $La_5Si_2BO_{13}$:Ce^{3+},Mn^{2+} phosphors, RSC Adv. 4 (2014) 7288–7295. https://doi.org/10.1039/C3RA47223J.

[55] J.R. Lakowicz, Principles of Fluorescence Spectroscopy, Springer Science & Business Media, 2007. ISBN 978-0-387-46312-4.
[56] B. Pahari, S. Chakraborty, B. Sengupta, S. Chaudhuri, W. Martin, J. Taylor, J. Henley, D. Davis, P.K. Biswas, A.K. Sharma, P.K. Sengupta, Biophysical Characterization of Genistein in Its Natural Carrier Human Hemoglobin Using Spectroscopic and Computational Approaches, Food and Nutrition Sciences 4 (2013) 83-92. https://doi.org/10.4236/fns.2013.48A011.
[57] F. Könz, Y. Sun, C.W. Thiel, R.L. Cone, R.W. Equall, R.L. Hutcheson, R.M. Macfarlane, Temperature and concentration dependence of optical dephasing, spectral-hole lifetime, and anisotropic absorption in Eu^{3+}:Y_2SiO_5, Phys. Rev. B. 68 (2003) 085109. https://doi.org/10.1103/PhysRevB.68.085109.
[58] G.E. Khalil, K. Lau, G.D. Phelan, B. Carlson, M. Gouterman, J.B. Callis, L.R. Dalton, Europium beta-diketonate temperature sensors: Effects of ligands, matrix, and concentration, Rev. Sci. Instrum. 75 (2004) 192–206. https://doi.org/10.1063/1.1632997.
[59] K. Maheshvaran, K. Marimuthu, Concentration dependent Eu^{3+} doped boro-tellurite glasses—Structural and optical investigations, J. Lumin. 9 (2012) 2259–2267. https://doi.org/10.1016/j.jlumin.2012.04.022.
[60] N. Bloembergen, Solid State Infrared Quantum Counters, Phys. Rev. Lett. 2 (1959) 84–85. https://doi.org/10.1103/PhysRevLett.2.84.
[61] F. Auzel, Compteur quantique par transfert d'énergie entre deux ions de terres rares dans un tungstate mixte et dans un verre, C. R. Acad. Sci. Paris 262 (1966) 1016–1019.
[62] M. Pollnau, D.R. Gamelin, S.R. Lüthi, H.U. Güdel, M.P. Hehlen, Power dependence of upconversion luminescence in lanthanide and transition-metal-ion systems, Phys. Rev. B. 61 (2000) 3337–3346. https://doi.org/10.1103/PhysRevB.61.3337.
[63] X. Cai, J.E. Martin, L.E. Shea-Rohwer, K. Gong, D.F. Kelley, Thermal Quenching Mechanisms in II–VI Semiconductor Nanocrystals, J. Phys. Chem. C. 117 (2013) 7902–7913. https://doi.org/10.1021/jp400688g.
[64] D.W. Cooke, B.L. Bennett, R.E. Muenchausen, J.-K. Lee, M.A. Nastasi, Intrinsic ultraviolet luminescence from Lu_2O_3, Lu_2SiO_5 and Lu_2SiO_5:Ce^{3+}, J. Lumin. 106 (2004) 125–132. https://doi.org/10.1016/j.jlumin.2003.09.001.
[65] Theoretical Basis of Luminescence Phenomena, in: Therm. Opt. Stimul. Lumin., John Wiley & Sons, Ltd, 2011: pp. 7–28. https://doi.org/10.1002/9781119993766.ch2.
[66] F. Sidiroglou, S. A. Wade, N. M. Dragomir, G. W. Baxter, S. F. Collins, Effects of high-temperature heat treatment on Nd^{3+}-doped optical fibers for use in fluorescence intensity ratio based temperature sensing. *Rev. Sci. Instrum.* 74, (2003) 3524–3530. https://doi.org/10.1063/1.1578706.
[67] X. Wang, X. Kong, Y. Yu, Y. Sun, H. Zhang, Effect of Annealing on Upconversion Luminescence of ZnO:Er^{3+} Nanocrystals and High Thermal Sensitivity. *J. Phys. Chem. C* 111, (2007) 15119–15124. https://doi.org/10.1021/jp0686689.
[68] X. Li, Effects of Er^{3+} concentration on down-/up-conversion luminescence and temperature sensing properties in $NaGdTiO_4$:Er^{3+}/Yb^{3+} phosphors. *Ceram. Int.* 42, (2016) 14710–14715. https://doi.org/10.1016/j.ceramint.2016.06.096.
[69] Z. Wang, G. Zhou, D. Jiang, S. Wang, Recent development of $A_2B_2O_7$ system transparent ceramics, J. Adv. Ceram. 7 (2018) 289–306. https://doi.org/10.1007/s40145-018-0287-z.
[70] A. Bayart, J.-F. Blach, M. Huvé, F. Blanchard, P. Roussel, R. Desfeux, S. Saitzek, Optical properties of $Ln_2Ti_2O_7$ (with Ln = La to Lu) thin films grown on (110)-SrTiO3 substrates by pulsed laser deposition, Opt. Mater. 92 (2019) 303–310. https://doi.org/10.1016/j.optmat.2019.04.049.

Figure captions

Figure 1. XRD patterns of $La_{2-x-y}Eu_xEr_yTi_2O_7$. The stars indicate the cubic/pyrochlore phases.

Figure 2. SEM images of (a) $La_{1.94}Eu_{0.05}Er_{0.01}Ti_2O_7$, (b) $La_{1.90}Eu_{0.05}Er_{0.05}Ti_2O_7$, (c) $La_{1.60}Eu_{0.10}Er_{0.30}Ti_2O_7$, (d) $La_{1.55}Eu_{0.40}Er_{0.05}Ti_2O_7$.

Figure 3. Diffuse reflectance UV-Visible spectra and Tauc plots for $La_{1.85}Eu_{0.10}Er_{0.05}Ti_2O_7$, $Er_2Ti_2O_7$ and $Eu_2Ti_2O_7$ oxides.

Figure 4. Luminescence properties of $La_{1.6}Eu_{0.10}Er_{0.30}Ti_2O_7$ oxide: (a) Room-temperature excitation spectra recorded in the range of 250 to 575 nm at λ_{em}=547.5 nm and λ_{em}=612.5 nm; (b) Room-temperature emission spectra recorded in the range of 450 to 800 nm at λ_{exc}=310 nm and λ_{exc}=377 nm.

Figure 5. a) Photographs highlighting emission color of $La_{2-x-y}Eu_xEr_yTi_2O_7$ oxides under excitation at 365 nm; b) Intensity evolution of $^5S_{3/2} \rightarrow {}^4I_{15/2}$ transition vs. y in $La_{1.90-y}Eu_{0.10}Er_yTi_2O_7$ oxides under λ_{exc}=310, 377 and 393 nm ; c) Intensities evolutions of $^5D_0 \rightarrow {}^7F_4$ and $^5D_0 \rightarrow {}^7F_2$ transitions vs. x in $La_{1.95-x}Eu_xEr_{0.05}Ti_2O_7$ oxides under λ_{exc}=310 and 377 393 nm ; d) Intensities evolutions of $^5D_0 \rightarrow {}^7F_4$ and $^5D_0 \rightarrow {}^7F_2$ transitions vs. y in in $La_{1.90-y}Eu_{0.10}Er_yTi_2O_7$ oxides under λ_{exc}=310 and 377 nm.

Figure 6. a) Photoluminescence decay curves of $La_{1.95-x}Eu_xEr_{0.05}Ti_2O_7$ oxides b) Evolution of the average lifetime as a function of the x value under an excitation of 393 nm.

Figure 7. a) 3D plot and b) 2D projection of CIE 1931 coordinates of $La_{1.95-x}Eu_xEr_{0.05}Ti_2O_7$ oxides; c) 3D plot and d) 2D projection of CIE 1931 coordinates of $La_{1.90-y}Eu_{0.10}Er_yTi_2O_7$.

Figure 8. Transmittance spectra of glass alone and glass loaded with 2% by weight of $La_{1.60}Eu_{0.30}Er_{0.10}Ti_2O_7$ oxide (inset, photograph of the glass wafer under natural light and under UV excitation).

Figure 9. a) Photographs highlighting the emission color variation of $La_{2-x-y}Eu_xEr_yTi_2O_7$ oxides under 785 nm laser excitation (40 mW) b) Upconversion emission spectra of $La_{1.85}Eu_{0.10}Er_{0.05}Ti_2O_7$ with two exciting laser (808 and 980 nm); c) Upconversion emission spectra of $La_{1.85}Eu_{0.10}Er_{0.05}Ti_2O_7$ (λ_{ex}=980 nm) at different laser power (from 0.05 W to 0.98 W) recorded at room temperature; d) Power dependence of upconversion luminescence from $^4S_{3/2} \rightarrow {}^4I_{15/2}$ and $^4F_{9/2} \rightarrow {}^4I_{15/2}$ transitions.

Figure 10. Upconversion decays curves performed for $^4F_{9/2} \rightarrow {}^4I_{15/2}$ transition and obtained under 808 and 980 nm laser excitation. The blue curve represents the Instrument Response Function (IRF) for a laser pulse at 808 nm.

Figure 11. a) Emission spectra (λ_{ex}=980 nm) vs. temperature of $La_{1.85}Eu_{0.10}Er_{0.05}Ti_2O_7$ oxide in a range of 77 to 500 K; b) Evolution of UC intensity as a function of the temperature for $^4F_{9/2} \rightarrow {}^4I_{15/2}$ transition (inset a plot of $\ln(I_0/I-1)$ as a function of 1/T for the determination of the activation energy).

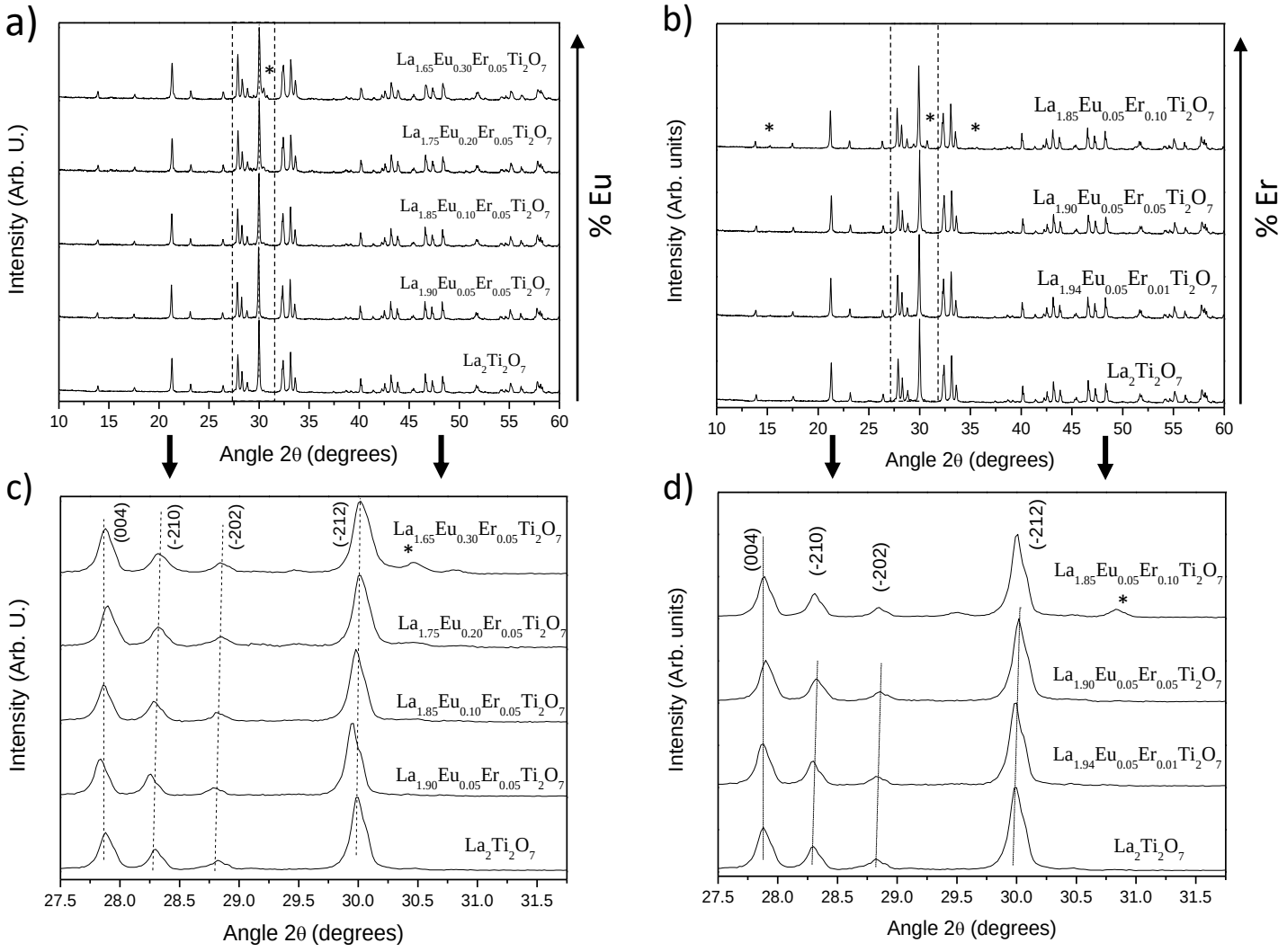
a)
Intensity (Arb. U.)
$La_{1.65}Eu_{0.30}Er_{0.05}Ti_2O_7$
$La_{1.75}Eu_{0.20}Er_{0.05}Ti_2O_7$
$La_{1.85}Eu_{0.10}Er_{0.05}Ti_2O_7$
$La_{1.90}Eu_{0.05}Er_{0.05}Ti_2O_7$
$La_2Ti_2O_7$
% Eu
Angle 2θ (degrees)
b)
Intensity (Arb. units)
$La_{1.85}Eu_{0.05}Er_{0.10}Ti_2O_7$
$La_{1.90}Eu_{0.05}Er_{0.05}Ti_2O_7$
$La_{1.94}Eu_{0.05}Er_{0.01}Ti_2O_7$
$La_2Ti_2O_7$
% Er
Angle 2θ (degrees)
c)
(004)
(-210)
(-202)
(-212)
Intensity (Arb. U.)
Angle 2θ (degrees)
d)
(004)
(-210)
(-202)
(-212)
Intensity (Arb. units)
Angle 2θ (degrees)

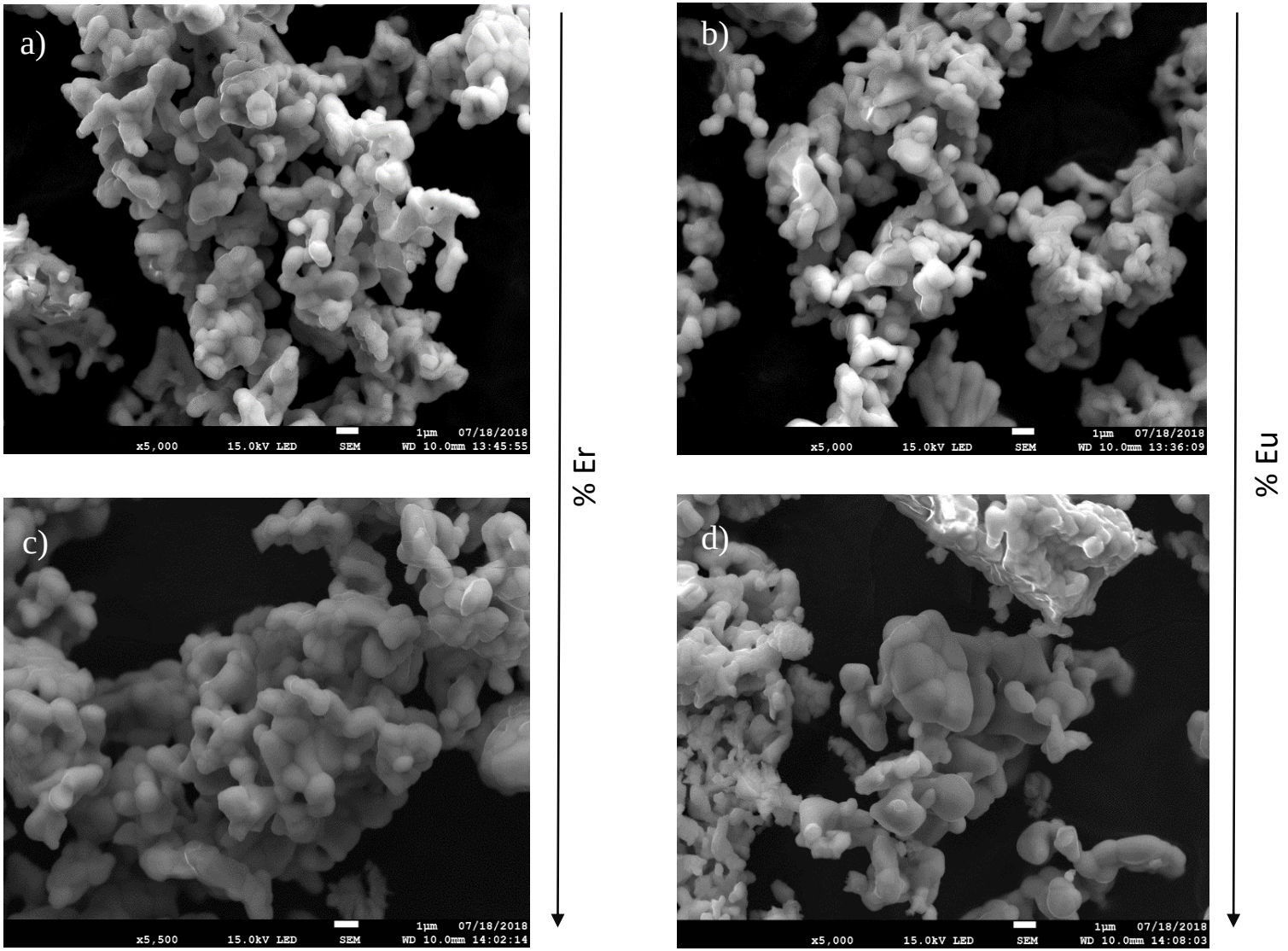
a)
x5,000 15.0kV LED SEM 1µm 07/18/2018 WD 10.0mm 13:45:55
b)
x5,000 15.0kV LED SEM 1µm 07/18/2018 WD 10.0mm 13:36:09
c)
x5,500 15.0kV LED SEM 1µm 07/18/2018 WD 10.0mm 14:02:14
d)
x5,000 15.0kV LED SEM 1µm 07/18/2018 WD 10.0mm 14:08:03
% Er
% Eu

a)

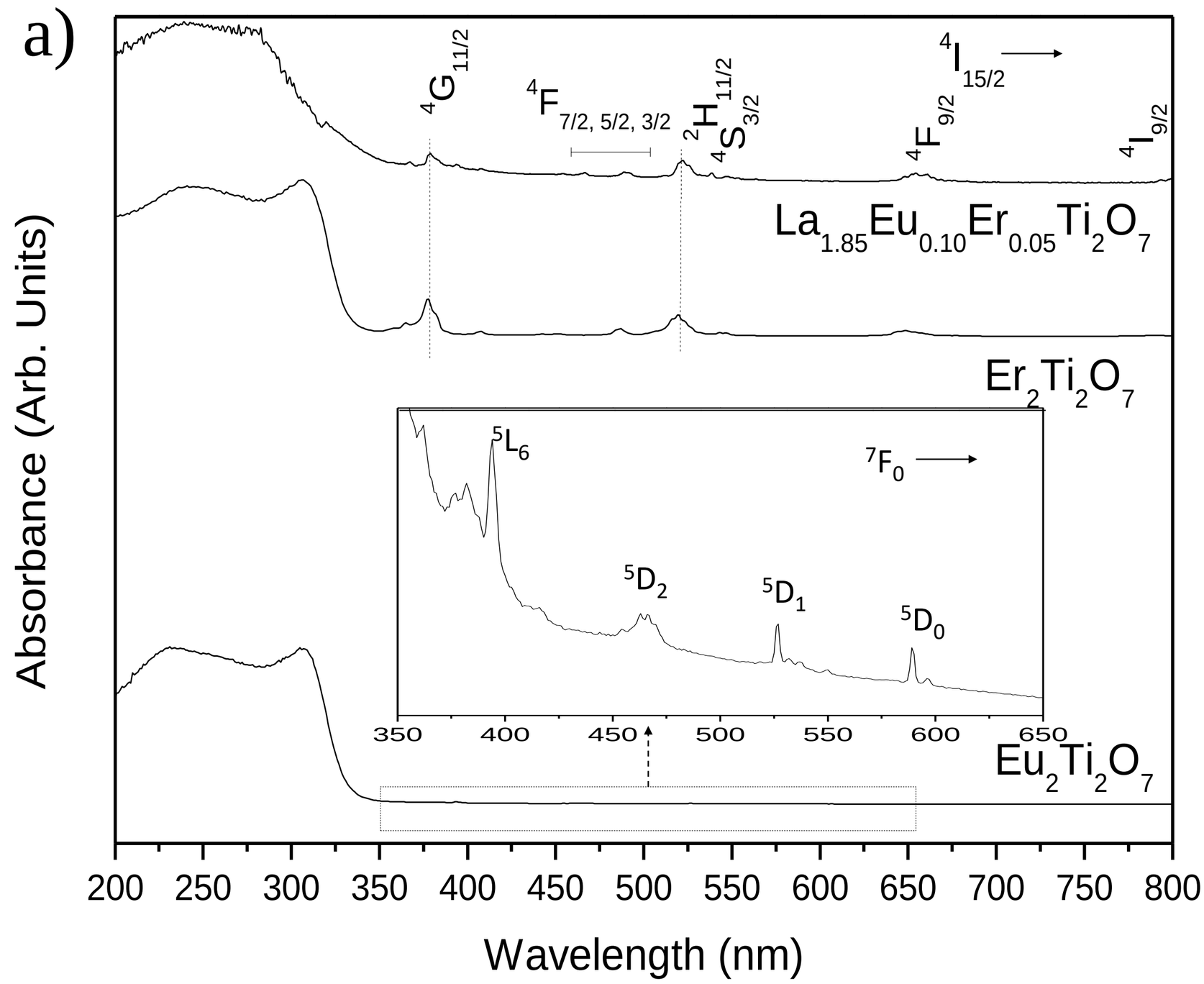
$^4G_{11/2}$
$^4F_{7/2, 5/2, 3/2}$
$^2H_{11/2}$
$^4S_{3/2}$
$^4F_{9/2}$
$^4I_{15/2}$
$^4I_{9/2}$
$La_{1.85}Eu_{0.10}Er_{0.05}Ti_2O_7$
$Er_2Ti_2O_7$
$^5L_6$
$^7F_0$
$^5D_2$
$^5D_1$
$^5D_0$
350 400 450 500 550 600 650
$Eu_2Ti_2O_7$
Absorbance (Arb. Units)
200 250 300 350 400 450 500 550 600 650 700 750 800
Wavelength (nm)

b)

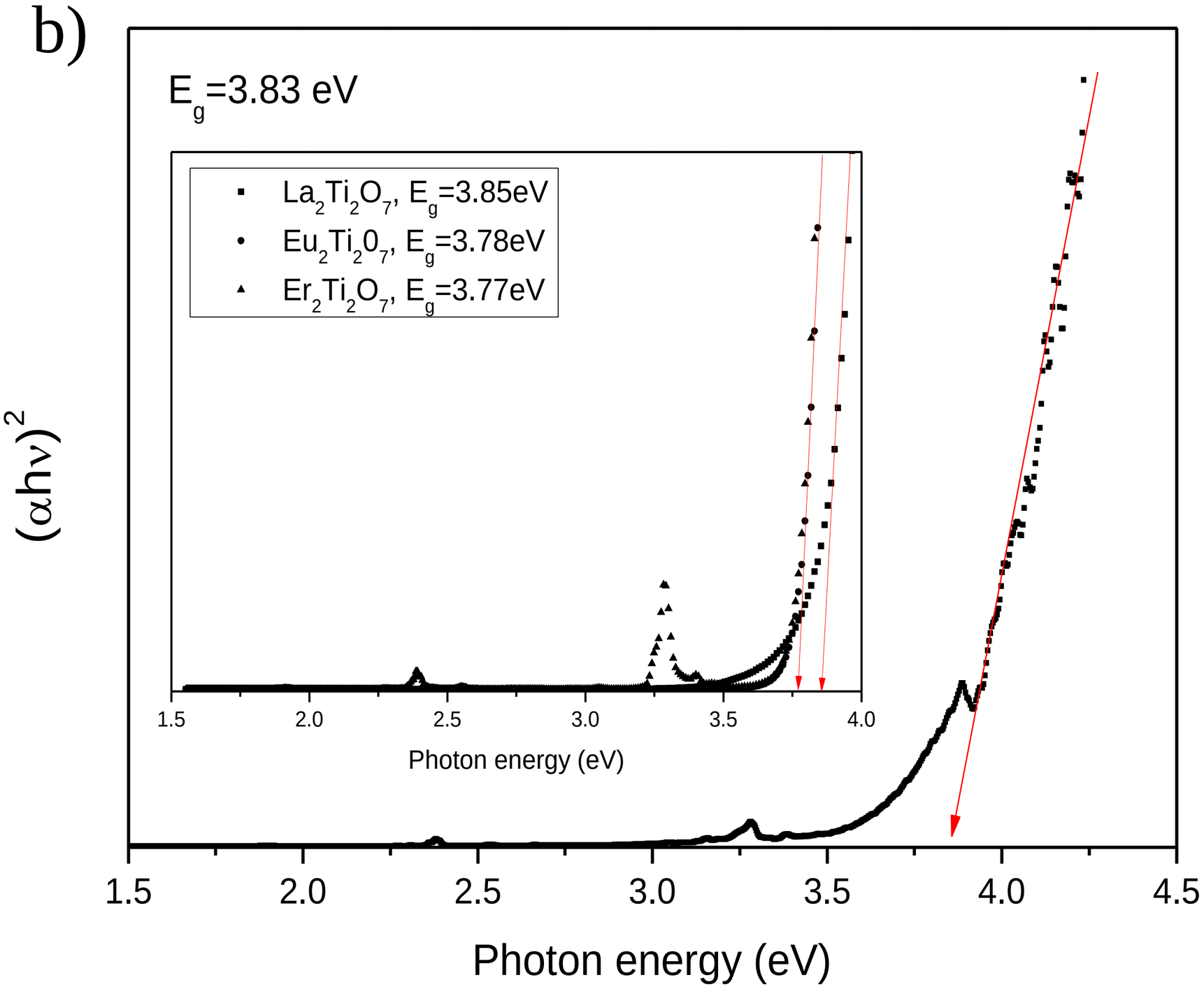
E_g=3.83 eV
$La_2Ti_2O_7$, E_g=3.85eV
$Eu_2Ti_20_7$, E_g=3.78eV
$Er_2Ti_2O_7$, E_g=3.77eV
1.5 2.0 2.5 3.0 3.5 4.0
Photon energy (eV)
$(\alpha h\nu)^2$
1.5 2.0 2.5 3.0 3.5 4.0 4.5
Photon energy (eV)

a)

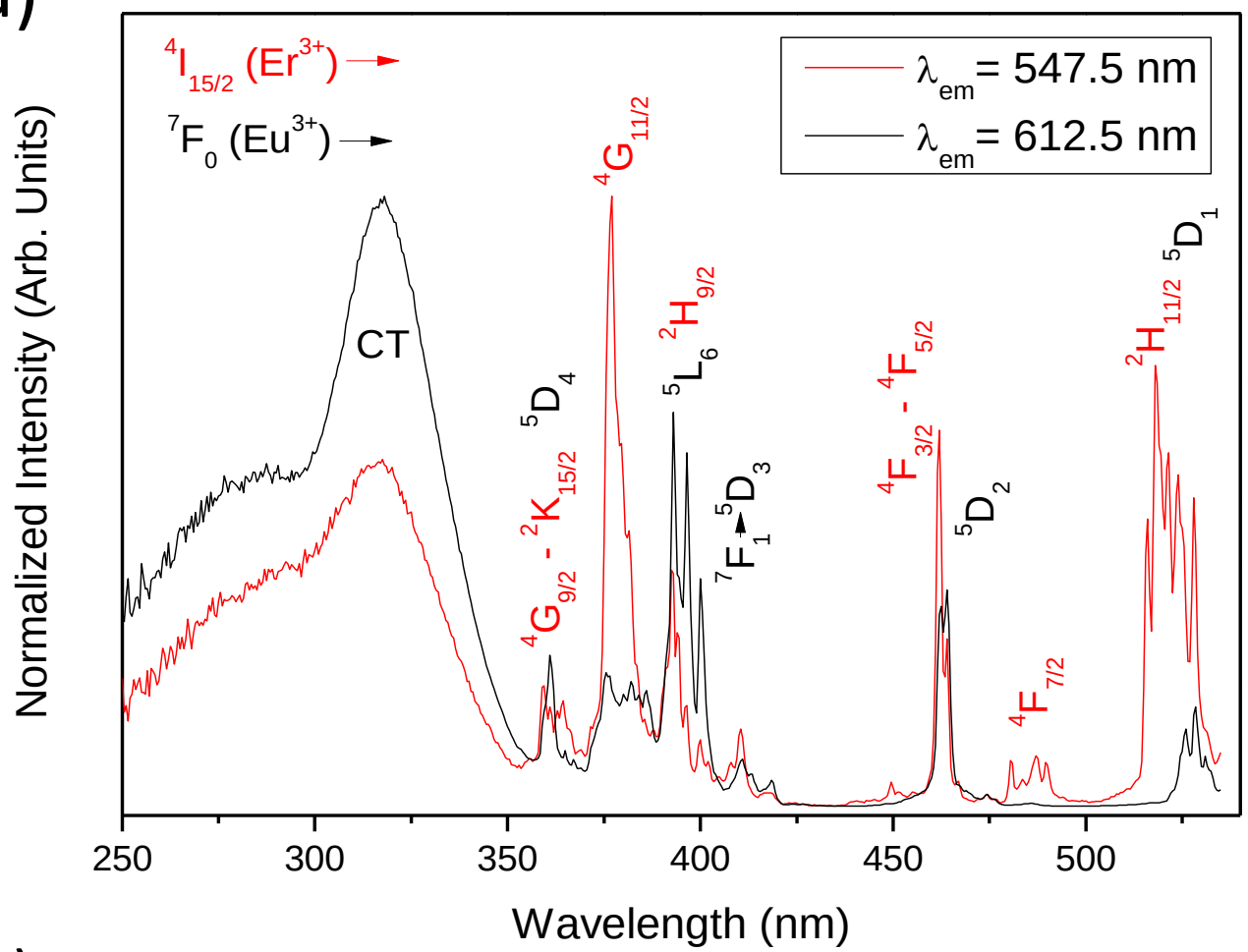
$^4I_{15/2}$ (Er^{3+})
$^7F_0$ (Eu^{3+})
λ_{em} = 547.5 nm
λ_{em} = 612.5 nm
CT
$^4G_{9/2}$ - $^2K_{15/2}$
$^5D_4$
$^4G_{11/2}$
$^5L_6$
$^2H_{9/2}$
$^7F_1$
$^5D_3$
$^4F_{3/2}$ - $^4F_{5/2}$
$^5D_2$
$^4F_{7/2}$
$^2H_{11/2}$
$^5D_1$
Normalized Intensity (Arb. Units)
250
300
350
400
450
500
Wavelength (nm)

b)

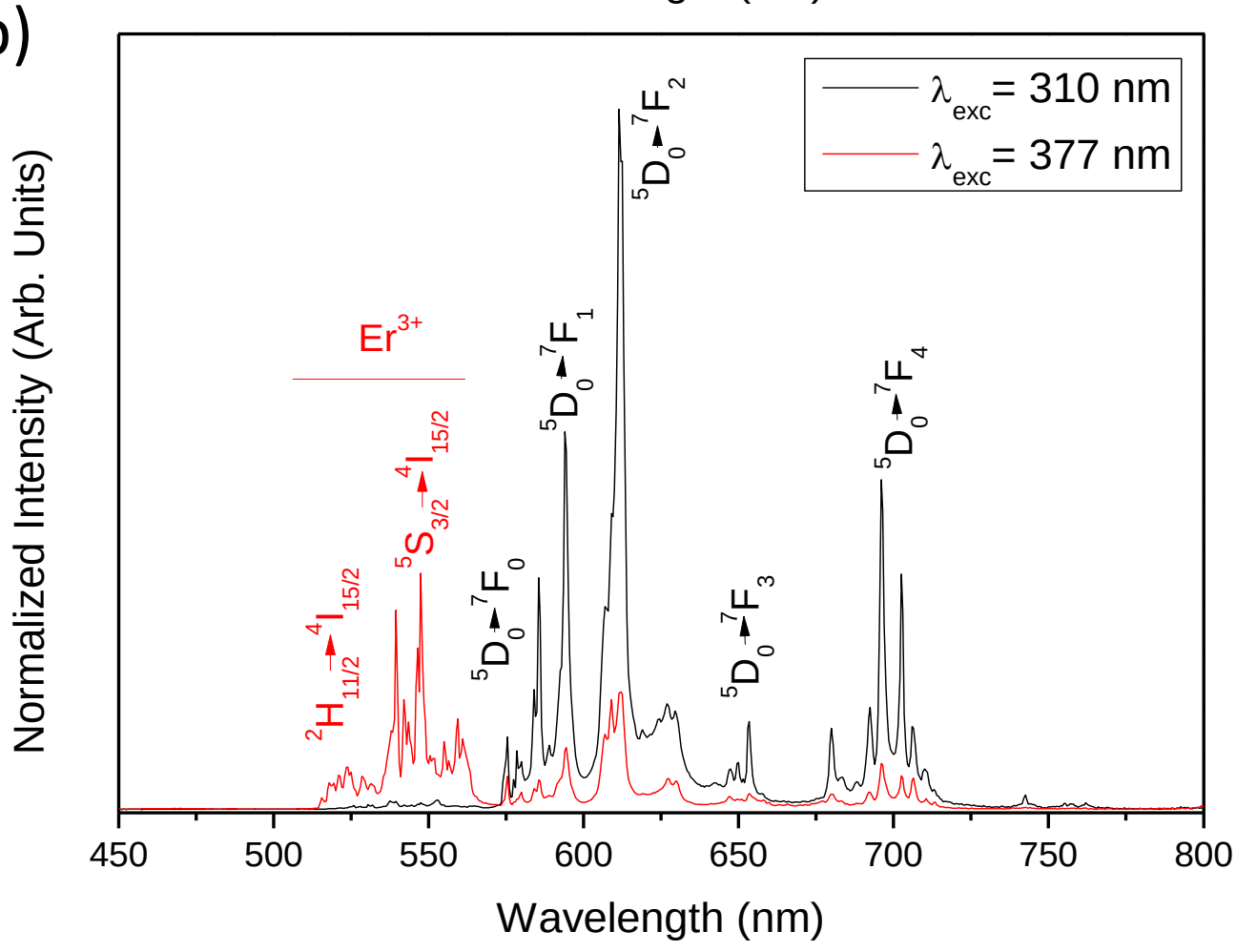
λ_{exc} = 310 nm
λ_{exc} = 377 nm
Er^{3+}
$^2H_{11/2} \rightarrow {}^4I_{15/2}$
$^5S_{3/2} \rightarrow {}^4I_{15/2}$
$^5D_0 \rightarrow {}^7F_0$
$^5D_0 \rightarrow {}^7F_1$
$^5D_0 \rightarrow {}^7F_2$
$^5D_0 \rightarrow {}^7F_3$
$^5D_0 \rightarrow {}^7F_4$
Normalized Intensity (Arb. Units)
450
500
550
600
650
700
750
800
Wavelength (nm)

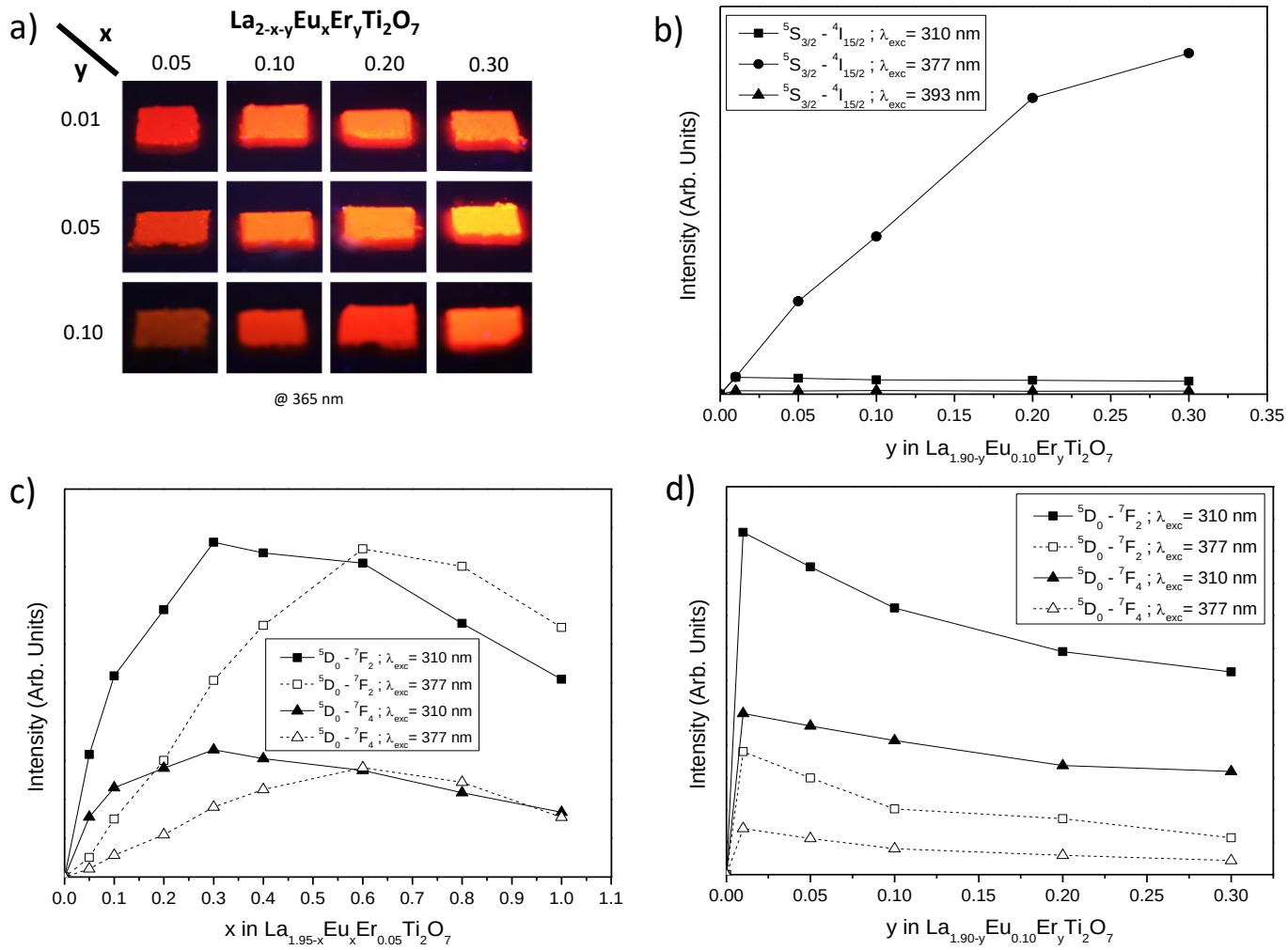
a)
La2-x-yEuxEryTi2O7
x
y
0.05
0.10
0.20
0.30
0.01
0.05
0.10
@ 365 nm
b)
5S3/2 - 4I15/2 ; λexc= 310 nm
5S3/2 - 4I15/2 ; λexc= 377 nm
5S3/2 - 4I15/2 ; λexc= 393 nm
Intensity (Arb. Units)
y in La1.90-yEu0.10EryTi2O7
c)
5D0 - 7F2 ; λexc= 310 nm
5D0 - 7F2 ; λexc= 377 nm
5D0 - 7F4 ; λexc= 310 nm
5D0 - 7F4 ; λexc= 377 nm
Intensity (Arb. Units)
x in La1.95-xEuxEr0.05Ti2O7
d)
5D0 - 7F2 ; λexc= 310 nm
5D0 - 7F2 ; λexc= 377 nm
5D0 - 7F4 ; λexc= 310 nm
5D0 - 7F4 ; λexc= 377 nm
Intensity (Arb. Units)
y in La1.90-yEu0.10EryTi2O7

a)

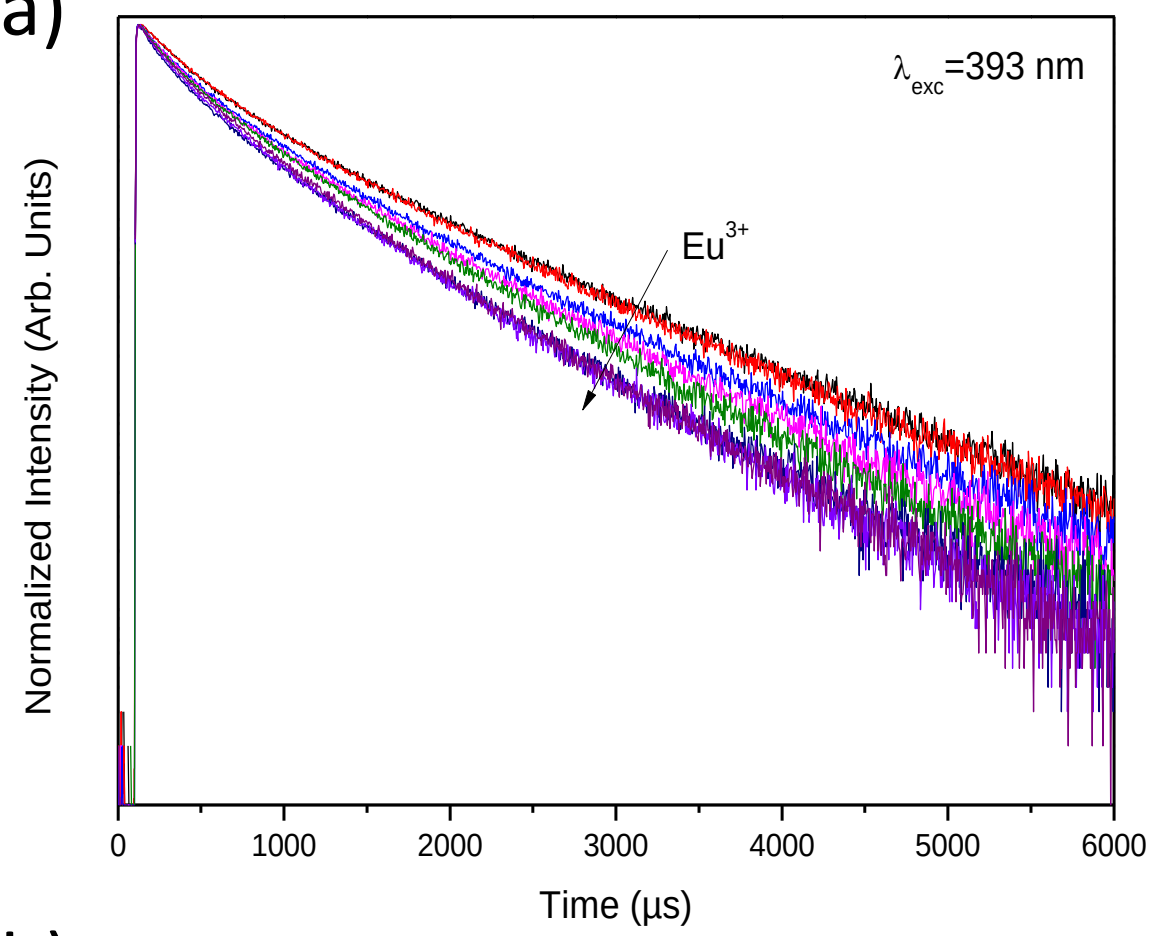
λexc=393 nm
Eu3+
Normalized Intensity (Arb. Units)
0
1000
2000
3000
4000
5000
6000
Time (μs)

b)

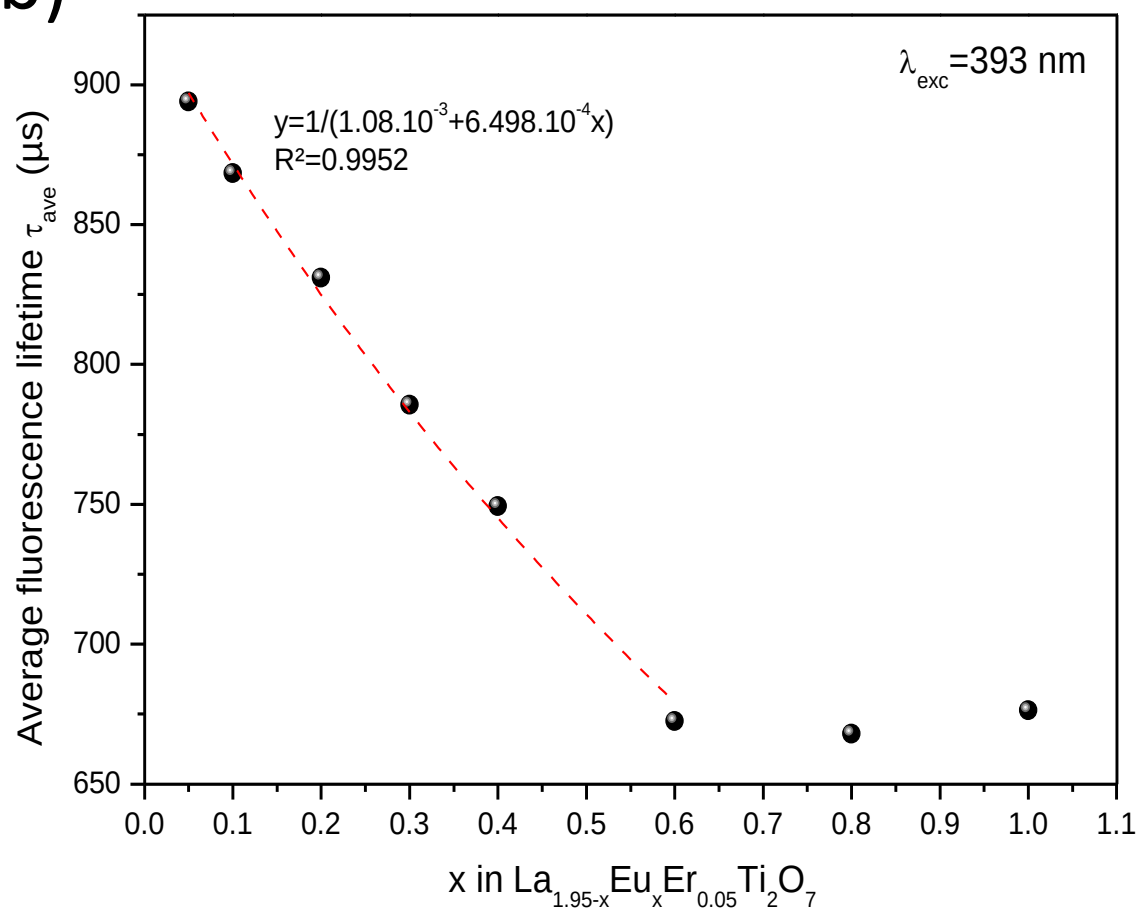
λexc=393 nm
y=1/(1.08.10-3+6.498.10-4x)
R²=0.9952
Average fluorescence lifetime τave (μs)
900
850
800
750
700
650
0.0
0.1
0.2
0.3
0.4
0.5
0.6
0.7
0.8
0.9
1.0
1.1
x in La1.95-xEuxEr0.05Ti2O7

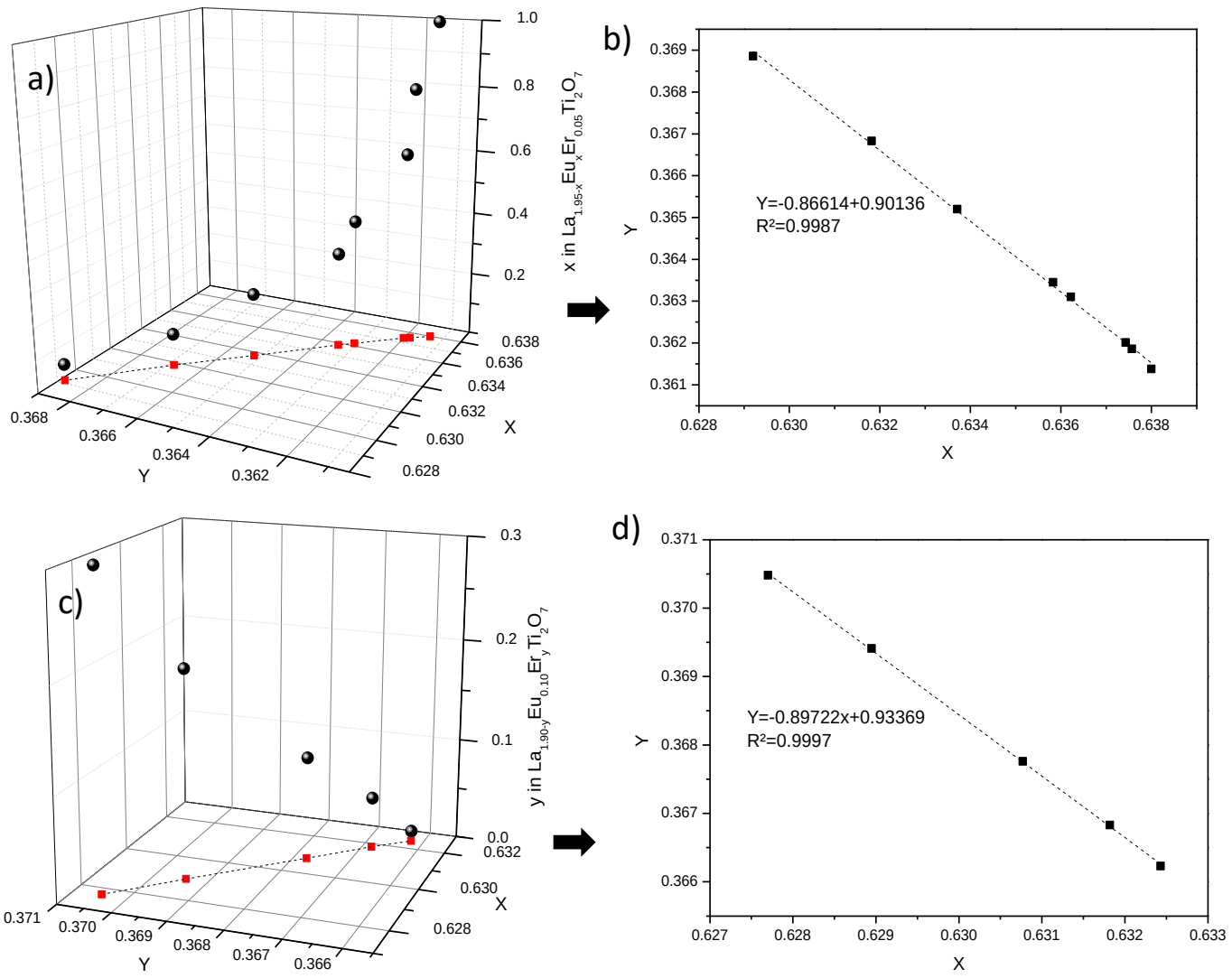
a)
1.0
0.8
0.6
0.4
0.2
x in $La_{1.95-x}Eu_xEr_{0.05}Ti_2O_7$
0.638
0.636
0.634
0.632
0.630
0.628
X
0.368
0.366
0.364
0.362
Y
b)
0.369
0.368
0.367
0.366
0.365
0.364
0.363
0.362
0.361
Y
Y=-0.86614+0.90136
R^2=0.9987
0.628
0.630
0.632
0.634
0.636
0.638
X
c)
0.3
0.2
0.1
0.0
y in $La_{1.90-y}Eu_{0.10}Er_yTi_2O_7$
0.632
0.630
0.628
X
0.371
0.370
0.369
0.368
0.367
0.366
Y
d)
0.371
0.370
0.369
0.368
0.367
0.366
Y
Y=-0.89722x+0.93369
R^2=0.9997
0.627
0.628
0.629
0.630
0.631
0.632
0.633
X

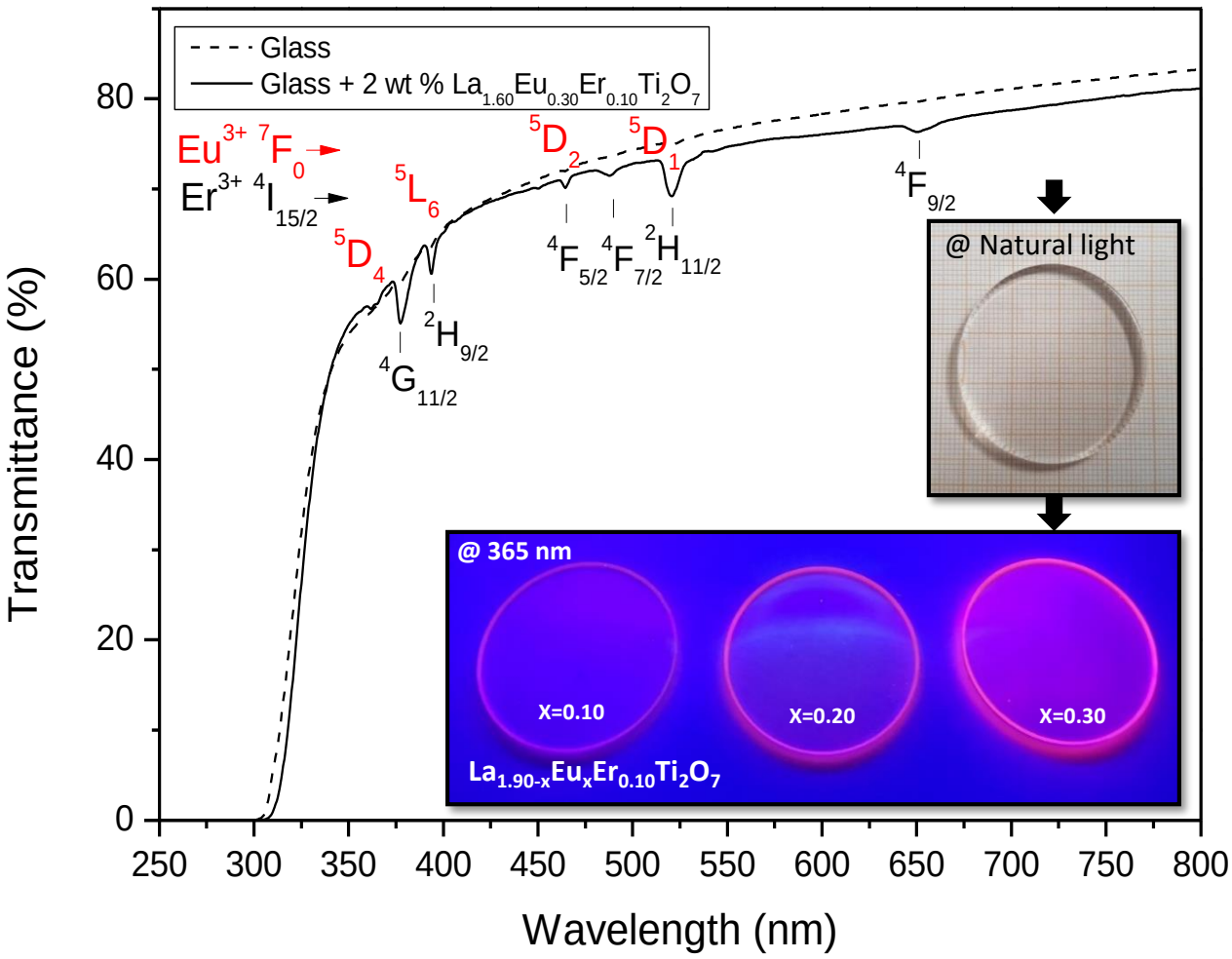
Glass
Glass + 2 wt % La1.60Eu0.30Er0.10Ti2O7
Eu3+ 7F0
Er3+ 4I15/2
5D4
5L6
4G11/2
2H9/2
5D2
4F5/2
4F7/2
2H11/2
5D1
4F9/2
@ Natural light
@ 365 nm
X=0.10
X=0.20
X=0.30
La1.90-xEuxEr0.10Ti2O7
Transmittance (%)
Wavelength (nm)
0
20
40
60
80
250
300
350
400
450
500
550
600
650
700
750
800

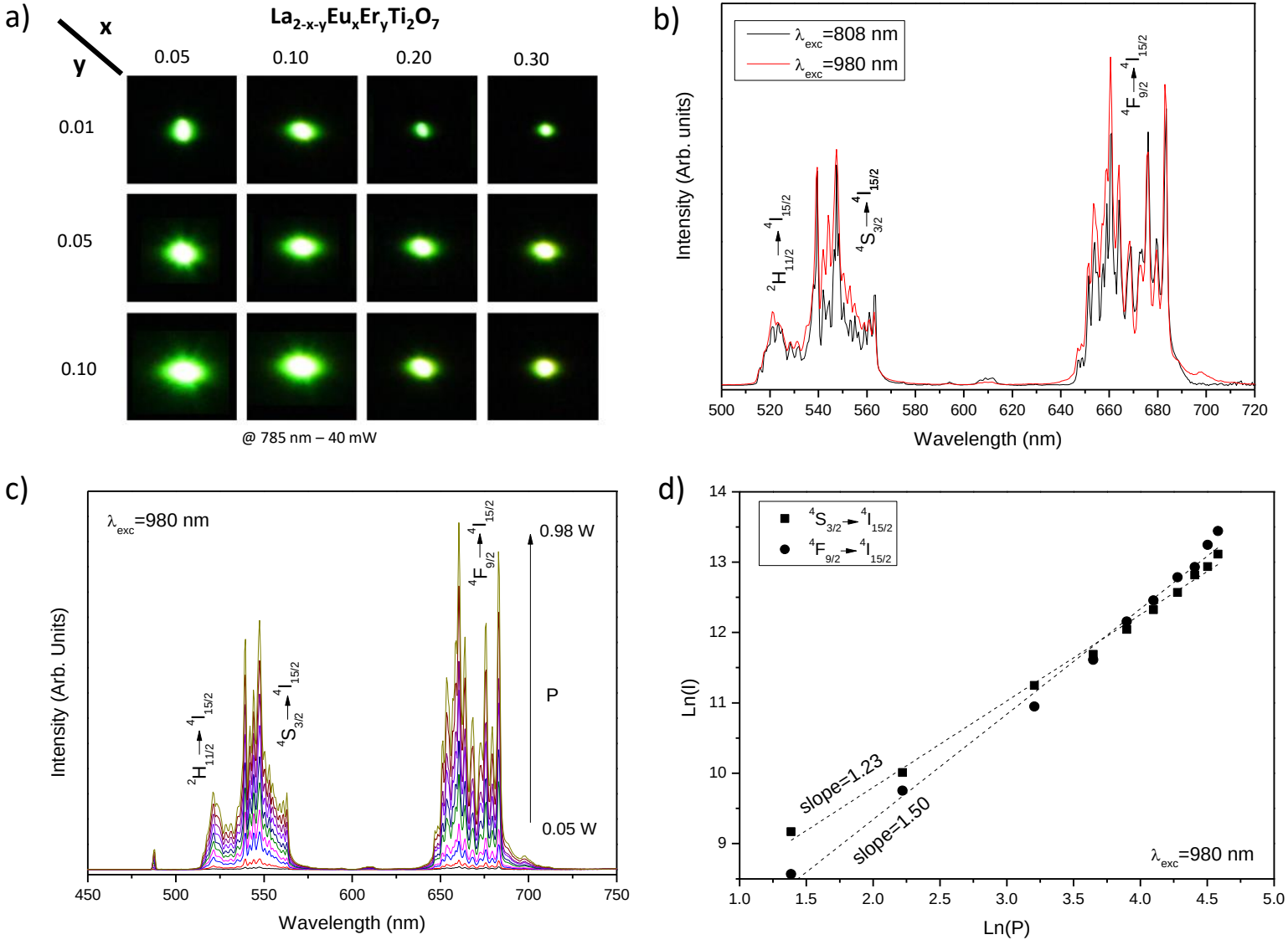
a)
$La_{2-x-y}Eu_xEr_yTi_2O_7$
x
y
0.05
0.10
0.20
0.30
0.01
0.05
0.10
@ 785 nm – 40 mW
b)
λ_{exc}=808 nm
λ_{exc}=980 nm
Intensity (Arb. units)
$^2H_{11/2} \rightarrow {}^4I_{15/2}$
$^4S_{3/2} \rightarrow {}^4I_{15/2}$
$^4F_{9/2} \rightarrow {}^4I_{15/2}$
500 520 540 560 580 600 620 640 660 680 700 720
Wavelength (nm)
c)
λ_{exc}=980 nm
0.98 W
P
0.05 W
Intensity (Arb. Units)
$^2H_{11/2} \rightarrow {}^4I_{15/2}$
$^4S_{3/2} \rightarrow {}^4I_{15/2}$
$^4F_{9/2} \rightarrow {}^4I_{15/2}$
450 500 550 600 650 700 750
Wavelength (nm)
d)
$^4S_{3/2} \rightarrow {}^4I_{15/2}$
$^4F_{9/2} \rightarrow {}^4I_{15/2}$
slope=1.23
slope=1.50
λ_{exc}=980 nm
Ln(I)
9 10 11 12 13 14
1.0 1.5 2.0 2.5 3.0 3.5 4.0 4.5 5.0
Ln(P)

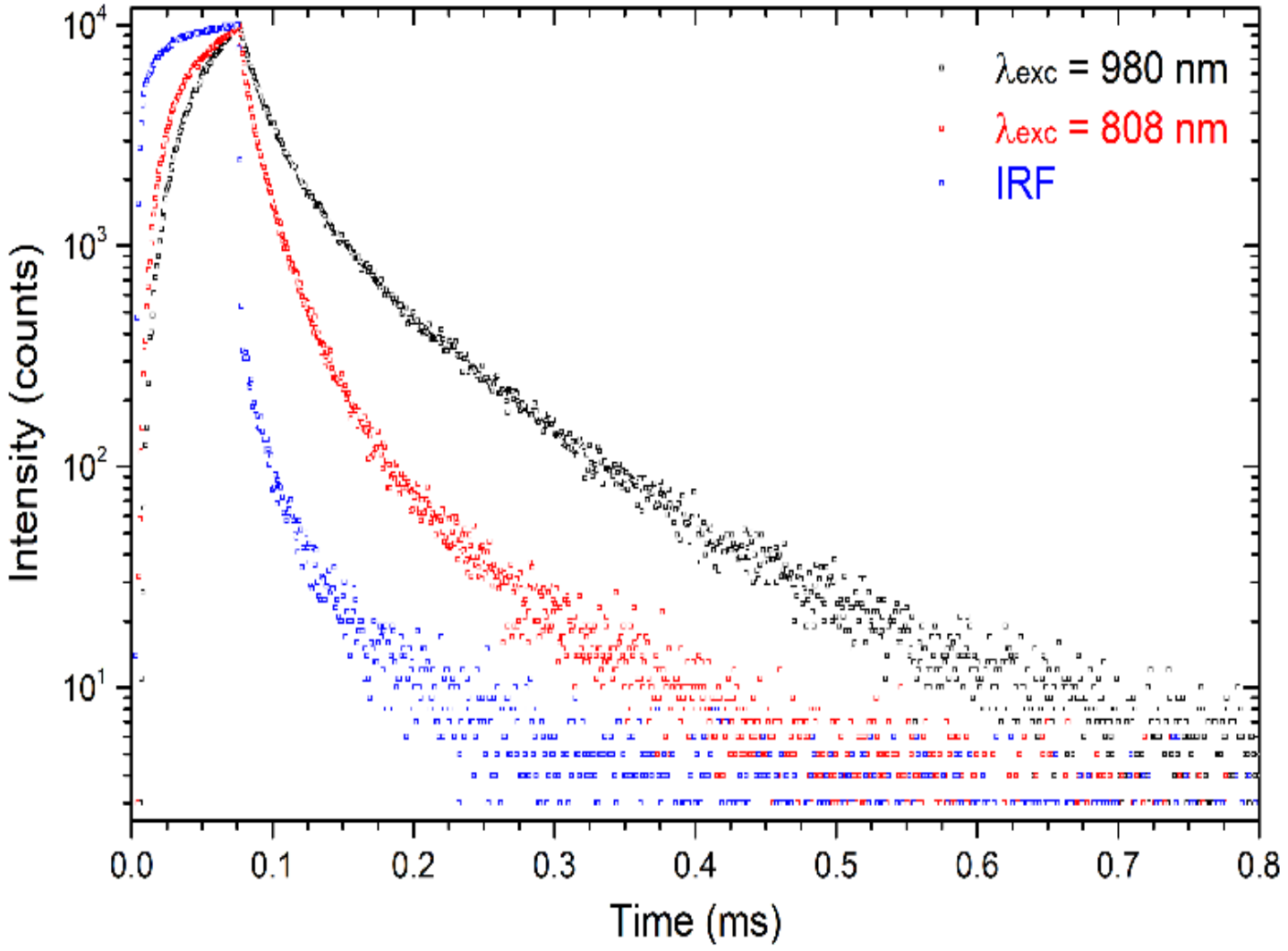
λexc = 980 nm
λexc = 808 nm
IRF
Intensity (counts)
Time (ms)
10^4
10^3
10^2
10^1
0.0
0.1
0.2
0.3
0.4
0.5
0.6
0.7
0.8

a)

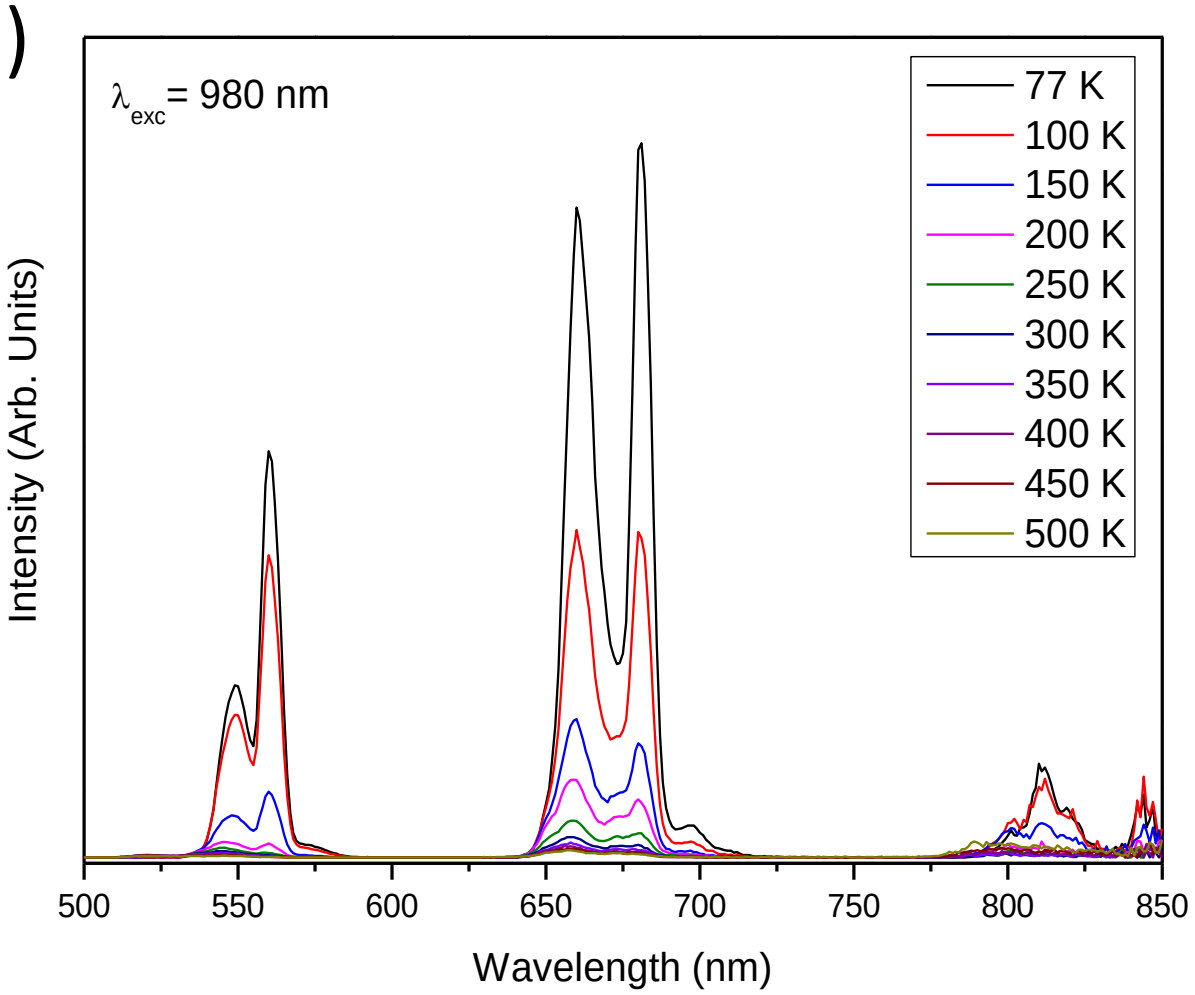
λexc = 980 nm
77 K
100 K
150 K
200 K
250 K
300 K
350 K
400 K
450 K
500 K
Intensity (Arb. Units)
500
550
600
650
700
750
800
850
Wavelength (nm)

b)

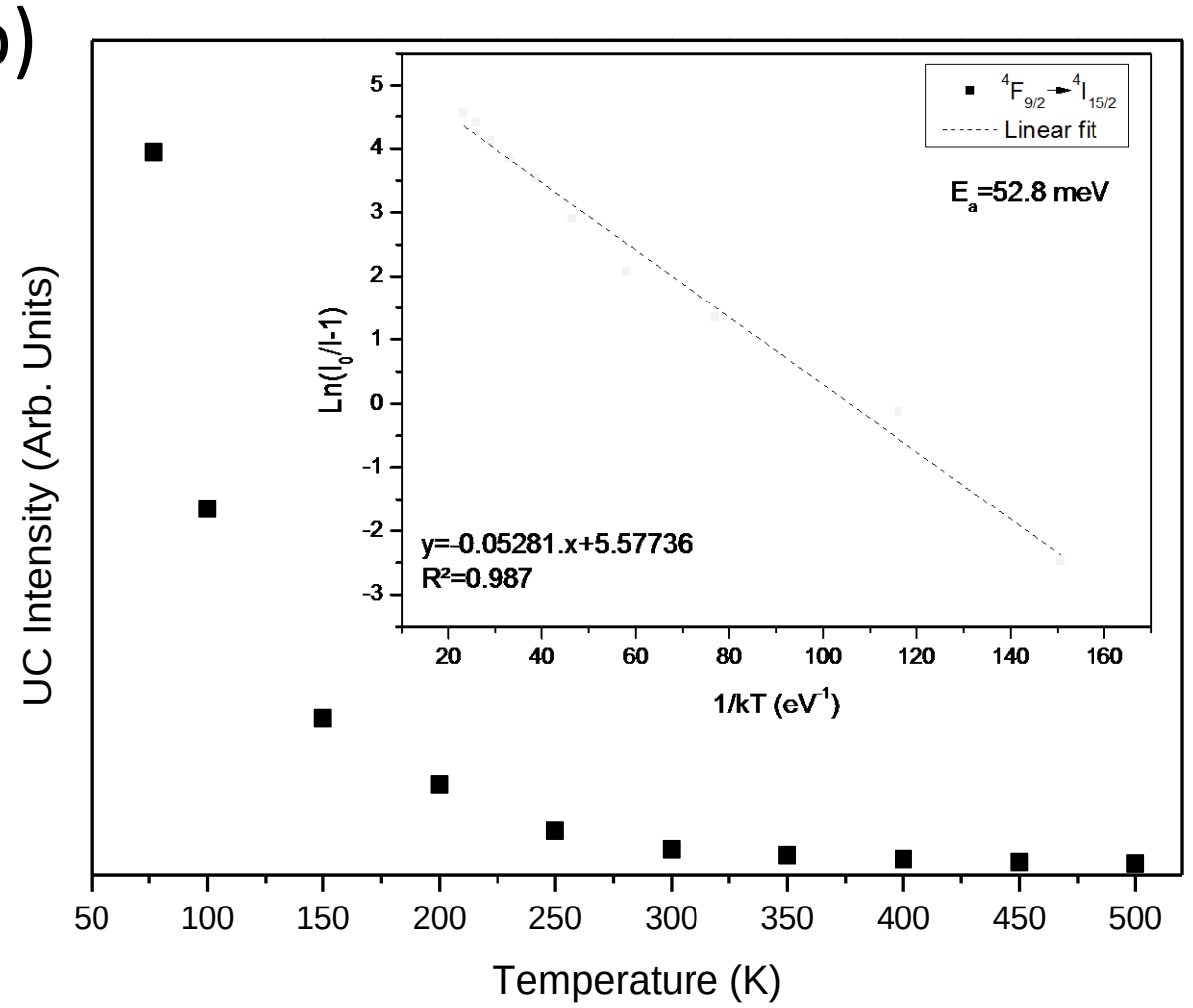
UC Intensity (Arb. Units)
50
100
150
200
250
300
350
400
450
500
Temperature (K)
4F9/2 → 4I15/2
Linear fit
Ea=52.8 meV
Ln(I0/I-1)
y=-0.05281.x+5.57736
R²=0.987
1/kT (eV-1)

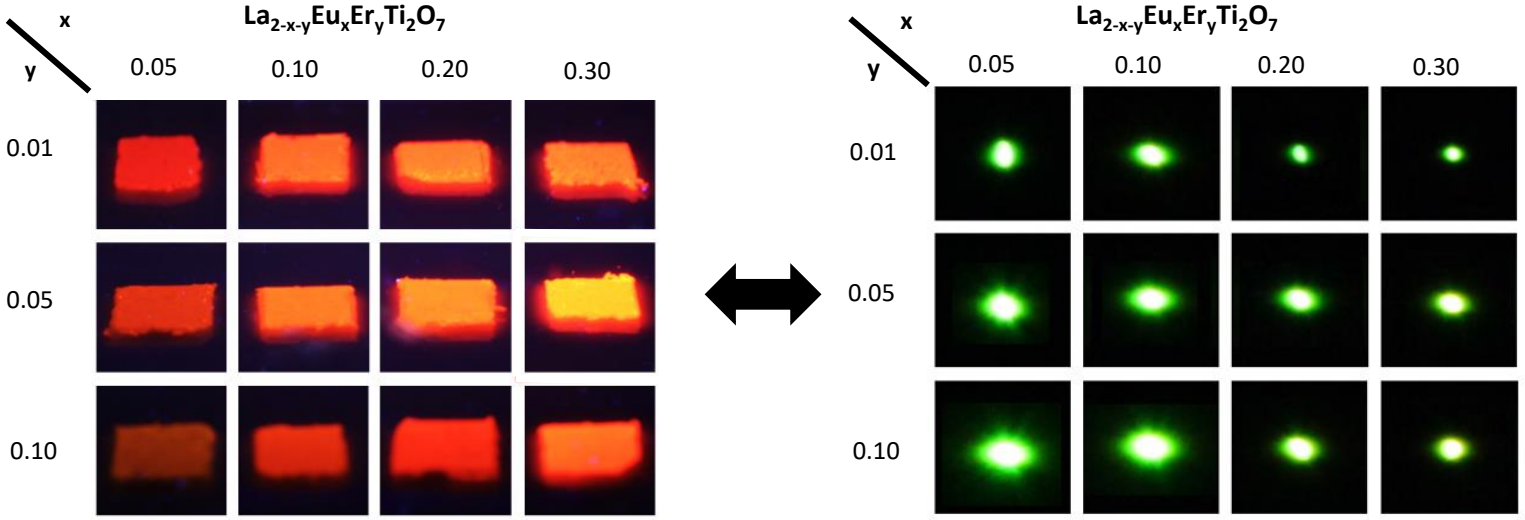

@ 365 nm

@ 785 nm – 40 mW